Statistical accuracy of scattered points filters and application to the dynamics of bubbles in gas-fluidized beds

Journal Article

Author(s):
Acosta-Iborra, A.; Sanchez-Delgado, S.; Scott, S. A.; Muller, C. R.; Dennis, J. S.

Statistical accuracy of scattered points filters and application to the dynamics of bubbles in gas-fluidized beds

A. Acosta-Iborra[1,†], **S. Sánchez-Delgado**[1], **S. A. Scott**[2], **C. R. Müller**[3] **and J. S. Dennis**[4]

[1]Department of Thermal and Fluid Engineering, Carlos III University of Madrid, Avda. de la Universidad 30, 28911 Leganés, Madrid, Spain

[2]Department of Engineering, University of Cambridge, Trumpington Street, Cambridge CB2 1PZ, UK

[3]Department of Mechanical Process Engineering, Swiss Federal Institute of Technology Zurich, Leonhardstrasse 27, LEO D7, 8092 Zurich, Switzerland

[4]Department of Chemical Engineering and Biotechnology, University of Cambridge, Pembroke Street, Cambridge CB2 3RA, UK

A novel analytical equation for the assessment of the accuracy of filters used for the interpolation and differentiation of scattered experimental data is presented. The equation takes into account the statistical nature of the filter output resulting from both the arbitrary positions of the data points and the randomness and noise present in the experimental data. Numerical estimation of the accuracy of the filter, using a Monte Carlo procedure, shows good agreement with the deduced analytical equation. This numerical procedure was also used to determine the accuracy of variance filters aimed at calculating the mean-square fluctuation of experimental data. The combination of the numerical results and analytical equations reveals the exact sources of inaccuracy arising in scattered point filters, namely: (i) the spectral inaccuracy of the weighting function; (ii) the noise or stochastic signal amplification; and (iii) the error arising from the random collocation of points within the filter window. The results also demonstrate that the use of the local mean in the calculation of the quadratic fluctuation leads to smaller estimation errors than the central mean. Finally, all these filters are used and critically evaluated in the framework of the stochastic position, diameter, and velocity of bubbles in a gas-fluidized bed. It is shown that the empirical coefficient of bubble coalescence in the two-dimensional bed tested, $\bar{\lambda}$, is in the range 2.0–2.4 when incorporating only the visible flow of bubbles. Here, the vertical distance over which a bubble survives without coalescing is $\bar{\lambda} L_c$, where L_c is the characteristic separation between neighbouring bubbles in the horizontal direction prior to coalescence. It was also seen that the relative mean-square-root fluctuation of both bubble diameter and velocity is more than 50 % at the centre of the bed and remains nearly constant along the height of the bed.

Key words: bubble dynamics, fluidized beds, particle/fluid flows

† Email address for correspondence: aacosta@ing.uc3m.es

1. Introduction

Experimental observations of many scientific and industrial systems often yield measurements made at discrete points, randomly positioned in temporal and spatial domains (Wendland 2005). This is especially true in the field of fluid mechanics measurements. For example, Imaichi & Ohmi (1983) measured the unsteady, incompressible, twin-vortex flow behind a cylinder using particle tracking velocimetry (PTV). The instantaneous velocities of the flow were acquired at scattered points in a two-dimensional section of the flow. More recently, a complete set of spatial derivatives of velocity in homogeneous turbulence was experimentally obtained by Lüthi, Tsinober & Kinzelbach (2005). They determined the stochastic trajectories of particles employing a three-dimensional PTV technique. Using a particle streak analysis, Orpe & Khakhar (2007) calculated the mean value, the spatial derivative and the root-mean square (r.m.s.) fluctuations of the particle velocity in a surface granular flow inside a rotating cylinder. Mattner, Joubert & Chong (2003) characterized the water velocity field past a sphere in a duct using laser Doppler velocimetry (LDV). Measurements were taken on grid points that were more concentrated in regions of large velocity gradients, and radial basis functions were used to produce analytic surface fits to the experimental velocity data. Other relevant applications concerning experimental or simulation data distributed at arbitrary points are, for instance, the study of the rheological behaviour of solid–liquid mixtures (Armanini *et al.* 2005), the evaluation of the turbulent diffusion of particles to a perfectly absorbing surface (Mann *et al.* 2005) or the characterization of bubble dynamics in liquids (Bunner & Tryggvason 2002).

In general, to extract information from such observations, the measurements have to be transformed or manipulated with data filters to allow, most commonly, interpolation (Imaichi & Ohmi 1983; Powell 1987; Wendland 2005) or, less commonly, differentiation (Malik & Dracos 1995; Lüthi *et al.* 2005; Wei & Li 2006; Nakamura, Wang & Wang 2008) and estimation of fluctuations (Vedula & Adrian 2005; Orpe & Khakhar 2007).

Although there have been many studies of the design and evaluation of filters for scattered points (e.g. Shepard 1968; Foley 1986; Agüí & Jiménez 1987; Powell 1987; Jackson 1989; Wendland 2005; Stickel 2009), the number concerned with the statistical accuracy of the filter output has been relatively few (Agüí & Jiménez 1987; Spedding & Rignot 1993; Malik & Dracos 1995; Lazzaro & Montefusco 2002; Vedula & Adrian 2005; Wei & Li 2006; Nakamura *et al.* 2008). In particular, to the authors' best knowledge, there has been no previous attempt to formulate expressions which elucidate analytically the obscure interactions among the truncation error, noise amplification and position randomness present in the filtering of experimental observations made at scattered points. Accordingly, the objective of the research presented in this paper is to improve the understanding of data filtering from scattered points by providing a methodology to estimate analytically the statistical accuracy of various filters. To do this, general closed-form expressions were derived to estimate the relative error associated with the operations of interpolation and direct differentiation of observations made at scattered points. Using four different types of filter, the results have been compared with estimates of error calculated numerically using a Monte Carlo method. The research also considers filters designed for the estimation of the mean-square fluctuation of stochastic data placed at scattered points. To illustrate the techniques applied to a practical system, an analysis was undertaken of experimental observations of bubbles in a gas–solid fluidized bed.

2. Filtering of observations made at scattered points

2.1. *Interpolation*

Without loss of generality, any continuum field, φ (e.g. pressure or fluid velocity), can be decomposed into a linear combination of a set of basis functions. In fluid mechanics this is typically performed via a Fourier transformation, which is particularly suited to identifying the different length scales of a flow system. Without loss of generality, the Fourier decomposition of φ is expressed here as a sine series:

$$\varphi(\boldsymbol{x}) = \sum_{L=0}^{\infty} \hat{\varphi}_L \prod_{i=1}^{D} \sin(x_i F_{i,l_i} + \psi_{i,l_i}). \tag{2.1}$$

Here D is the number of dimensions in the data field, $\boldsymbol{x} = [x_1, x_2, \ldots, x_D]$ is the coordinates vector, $\boldsymbol{L} = [l_1, l_2, \ldots, l_D]$ is the vector containing the Fourier index for each coordinate, ψ_{i,l_i} is the phase of the coordinate i for the Fourier component of index l_i and

$$F_{i,l_i} = \frac{2\pi}{S_i} l_i = \frac{2\pi}{\lambda_i} \tag{2.2}$$

is the Fourier frequency for the i coordinate and index l_i. In (2.2), S_i is the length of the domain along the i coordinate and $\lambda_i = S_i/l_i$ is its Fourier spatial wavelength. For example, in a two-dimensional field with $\boldsymbol{x} = [x, y]$ and $\boldsymbol{L} = [l, r]$, (2.1) becomes:

$$\varphi(x, y) = \sum_{l,r=0}^{\infty} \hat{\varphi}_{l,r} \sin(x F_{x,l} + \psi_{x,l}) \sin(y F_{y,r} + \psi_{y,r}). \tag{2.3}$$

The data to be filtered are the result of sampling φ at N_t randomly positioned points, $\boldsymbol{x}_k$, where $k = 1, 2, \ldots, N_t$. This sampling generates a scattered data field, ϕ, i.e. the measured data. The result can also be affected by measurement noise or other stochastic variation, ε_k, present at $\boldsymbol{x}_k$. Then, for each point, the measured data can be expressed as:

$$\phi_k = \varphi(\boldsymbol{x}_k) + \varepsilon_k. \tag{2.4}$$

Assuming that the noise, or any stochastic component of the data, has zero mean, $\langle \varepsilon_k \rangle_\varepsilon = 0$, and, for the worst case, is uncorrelated for any two different points, i and j, then:

$$\langle \varepsilon_i \varepsilon_j \rangle_\varepsilon = \begin{cases} \sigma_\varepsilon^2, & i = j \\ 0, & i \neq j \end{cases} \tag{2.5}$$

where $\langle \cdot \rangle_\varepsilon$ indicates the statistical average over all the possible realizations for the random signal ε, and σ_ε is the standard deviation of ε.

The filtering of data to obtain, for example, its interpolation, differentiation or mean fluctuating value, at an arbitrary point $\boldsymbol{x}$, can be undertaken using the local-averaging filter of Anderson & Jackson (1967) and Jackson (2000):

$$\tilde{\phi}(\boldsymbol{x}) = \frac{\displaystyle\sum_{k=1}^{N_p} g_*(\boldsymbol{x}_k - \boldsymbol{x}) \phi_k}{\displaystyle\sum_{k=1}^{N_p} g_*(\boldsymbol{x}_k - \boldsymbol{x})} \tag{2.6}$$
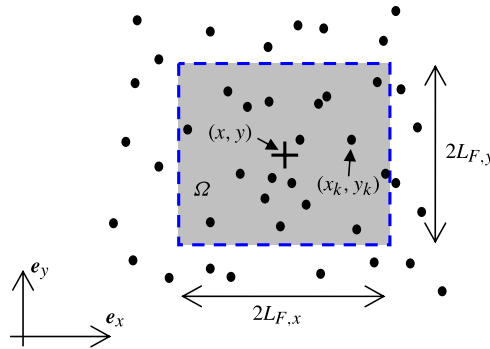
FIGURE 1. (Colour online) Rectangular window (shaded area Ω_F) used by the weighting function of a two-dimensional filter in a field with scattered data points.

where g_* is the weighting function used for the filtering and $\tilde{\phi}$ the value at the centre of the filter resulting from the filtering of the measured data ϕ_k. In (2.6), N_p is the number of points affected by the filter window, namely points for which g_* is non-zero. This is exemplified in figure 1 for a two-dimensional data field and a filter window covering a domain Ω_F of rectangular shape $2L_{F,x} \times 2L_{F,y}$. In this figure, the centre of the filter is marked with a cross at the point $\boldsymbol{x} = (x, y)$. The coordinates $\boldsymbol{x}_k = (x_k, y_k)$ of an arbitrary point represented by a dot are also shown.

For the particular case of interpolation, and following Anderson & Jackson (1967), the weighting function, g_I, can be normalized so that its integral in the D-dimensional space within the region Ω_F, is unity:

$$\int_{\Omega_F} g_I(\boldsymbol{x}) \, \mathrm{d}\boldsymbol{x} = 1. \tag{2.7}$$

This normalization is convenient since, as explained in Anderson & Jackson (1967), g_I directly leads to the local number density of sampling points at the filter centre, $n(\boldsymbol{x})$. Besides, provided a sufficiently large number of points is affected by the filter, the following approximation holds:

$$n(\boldsymbol{x}) = \sum_{k=1}^{N_p} g_I(\boldsymbol{x}_k - \boldsymbol{x}) \approx \frac{N_p}{V_F} \tag{2.8}$$

where $V_F = \int_{\Omega_F} \mathrm{d}\boldsymbol{x}$ is the area or volume of the filter window. Implicit in this approximation is the fact that the randomly positioned points, $\boldsymbol{x}$, can be in any part of Ω_F with equal probability, namely are homogeneously distributed in Ω_F. In other words, the bulk number density of sampling points on the left-hand side of (2.8) can be considered equal to the local number density if the macroscopic length scale for the spatial variation of $n(\boldsymbol{x})$ is much greater than the size of the filter window (Jackson 2000). Then

$$\tilde{\phi}(\boldsymbol{x}) = \frac{V_F \displaystyle\sum_{k=1}^{N_p} g_I(\boldsymbol{x}_k - \boldsymbol{x})\phi_k}{N_p}. \tag{2.9}$$

Interpolative filters can be readily generated from basic functions. The only restriction that will be imposed in the present analysis is that g_I must be continuous
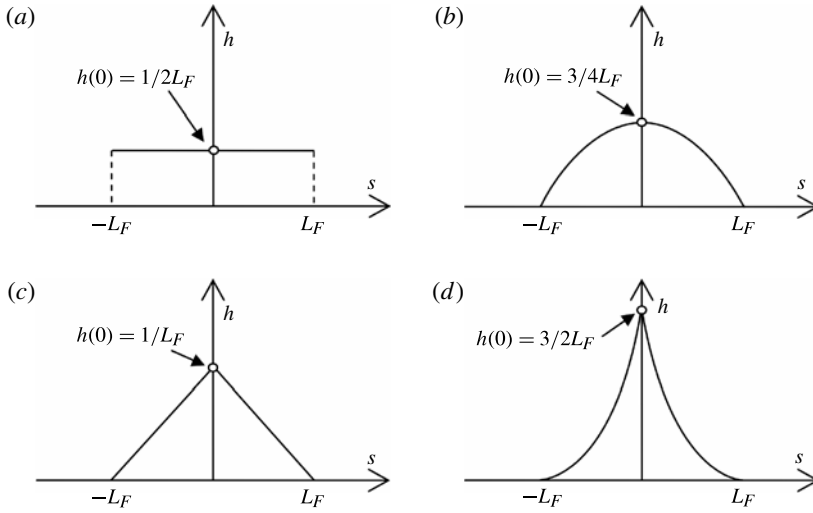
FIGURE 2. Examples of basic weighting functions of interpolative filters acting on rectangular windows: (*a*) constant; (*b*) parabolic dome; (*c*) pyramid; and (*d*) parabolic peak.

Source	$h(s)$, $s \in [-L_F, L_F]$
Constant profile	$\dfrac{1}{2L_F}$
Parabolic dome	$\dfrac{3}{4L_F}\left[1-\left(\dfrac{s}{L_F}\right)^2\right]$
Pyramid	$\dfrac{1}{L_F}\left[1-\left|\dfrac{s}{L_F}\right|\right]$
Parabolic peak	$\dfrac{3}{2L_F}\left[1-\left|\dfrac{s}{L_F}\right|\right]^2$

TABLE 1. Examples of basic functions $h(s)$ for interpolative weighting functions.

at all points in the interior of Ω_F. Figure 2 and table 1 present some examples of basic functions, $h(s)$, for the generation of g_I in a circular ($D = 2$) or spherical ($D = 3$) window with radius R_F, where

$$g_I(\boldsymbol{x}_k - \boldsymbol{x}) = \frac{h(|\boldsymbol{x}_k - \boldsymbol{x}|)}{2^{D-1}\pi \displaystyle\int_0^{R_F} h(r)r^{D-1}\,\mathrm{d}r}. \tag{2.10}$$

Alternatively, for a rectangular or square-section prismatic window,

$$g_I(\boldsymbol{x}_k - \boldsymbol{x}) = \prod_{i=1}^{D} h(x_{i,k} - x_i), \tag{2.11}$$

in which no normalization is needed, because $\int_{-L_F}^{L_F} h(s) \, \mathrm{d}s = 1$ for the basic functions presented in table 1. These basic functions are symmetrical with respect to $s = 0$ so that g_I is also symmetrical along any of the spatial coordinates covered by Ω_F.

2.2. *Differentiation*

The differentiation of data from randomly positioned points can be performed by differentiating the measured data (2.6):

$$\frac{\partial \tilde{\phi}(\boldsymbol{x})}{\partial x_1} = \frac{\displaystyle\sum_{k=1}^{N_p} \frac{\partial g_I(\boldsymbol{x}_k - \boldsymbol{x})}{\partial x_1} \phi_k}{\displaystyle\sum_{k=1}^{N_p} g_I(\boldsymbol{x}_k - \boldsymbol{x})} - \sum_{k=1}^{N_p} g_I(\boldsymbol{x}_k - \boldsymbol{x}) \phi_k \frac{\displaystyle\sum_{s=1}^{N_p} \frac{\partial g_I(\boldsymbol{x}_s - \boldsymbol{x})}{\partial x_1}}{\left(\displaystyle\sum_{s=1}^{N_p} g_I(\boldsymbol{x}_s - \boldsymbol{x})\right)^2} \quad (2.12)$$

where x_1 is the coordinate arbitrarily chosen from $\boldsymbol{x}$ for the differentiation. Letting $g_D(\boldsymbol{x}_k - \boldsymbol{x}) \equiv \partial g_I(\boldsymbol{x}_k - \boldsymbol{x})/\partial x_1$, the right-hand side of (2.12) can be written:

$$\frac{\displaystyle\sum_{k=1}^{N_p} g_D(\boldsymbol{x}_k - \boldsymbol{x}) \left[\phi_k - \tilde{\phi}(\boldsymbol{x})\right]}{\displaystyle\sum_{k=1}^{N_p} g_I(\boldsymbol{x}_k - \boldsymbol{x})}. \quad (2.13)$$

However, (2.12) can be greatly simplified using the approximation described by (2.8). In fact, the second term in the right-hand side of (2.12) is usually smaller than the first term owing to the symmetry of g_I which implies the anti-symmetry of g_D and leads to $\sum_{k=1}^{N_p} g_D(\boldsymbol{x}_k - \boldsymbol{x}) \to 0$ when $N_p \to \infty$. Thus, the following simplification can be used without affecting the results of filtering markedly:

$$\frac{\displaystyle\sum_{k=1}^{N_p} g_I(\boldsymbol{x}_k - \boldsymbol{x}) \phi_k}{\displaystyle\sum_{k=1}^{N_p} g_I(\boldsymbol{x}_k - \boldsymbol{x})} \approx \frac{\displaystyle\sum_{k=1}^{N_p} \phi_k}{N_p}, \quad (2.14)$$

so that

$$\frac{\partial \tilde{\phi}(\boldsymbol{x})}{\partial x_1} \approx \frac{\displaystyle\sum_{k=1}^{N_p} \left[g_D(\boldsymbol{x}_k - \boldsymbol{x}) \left(\phi_k - \frac{1}{N_p} \sum_{s=1}^{N_p} \phi_s\right)\right]}{\displaystyle\sum_{k=1}^{N_p} g_I(\boldsymbol{x}_k - \boldsymbol{x})}. \quad (2.15)$$

In the above, it becomes clear that $g_D(\boldsymbol{x}_k - \boldsymbol{x}) \equiv \partial g_I(\boldsymbol{x}_k - \boldsymbol{x})/\partial x_1$ is the weighting function for the differentiation filter. Note that (2.14) is obtained by making the simplification that g_I is constant, i.e. it is constructed with the constant-profile basic function shown in table 1. Alternative approximations for g_I in (2.14) are possible by selecting other basic functions from table 1. In the same way g_I in the denominator of (2.15) may be simplified. Of all the simplifications tested for (2.12), the one shown

Source	$h'(s), \ s \in [-L_F, L_F]^a$
Constant profile	$\dfrac{1}{2L_F} \left[\delta_D(x + L_F) - \delta_D(x - L_F) \right]$
Parabolic dome	$-\dfrac{3}{2L_F^2} \left(\dfrac{s}{L_F} \right)$
Pyramid	$-\dfrac{1}{L_F^2} \dfrac{|s|}{s} \quad s \neq 0$
Parabolic peak	$-\dfrac{3}{L_F^2} \dfrac{|s|}{s} \left[1 - \left| \dfrac{s}{L_F} \right| \right] \quad s \neq 0$

TABLE 2. Examples of basic functions $h'(s)$ for differentiation weighting functions. [a] For all the functions $h'(0) = 0$.

in (2.15) yielded the best results. For the particular case of rectangular or quadrilateral filter windows, the weighting function can be decomposed using (2.11):

$$g_D(\boldsymbol{x}_k - \boldsymbol{x}) = -h'(x_{1,k} - x_1) \prod_{i=2}^{D} h(x_{i,k} - x_i) \qquad (2.16)$$

where $h'(s) = \mathrm{d}h(s)/\mathrm{d}s$. Table 2 presents some examples of basic functions h' for g_D calculated with h taken from table 1. The value of h' when $s = 0$ can be equated to zero when h' has a discontinuity at that point. It can be seen that when the source function has a constant profile, the derivative is composed of two Dirac functions δ_D: the resulting filter is impracticable since it would produce singularities in the filtered data.

2.3. *Variance*

It might be necessary to quantify the variance or mean quadratic fluctuation, υ^2, of the field φ over its mean μ. Of course, this depends on how the data mean is defined and calculated. Here, the case will be considered in which the fluctuation is: (i) uncorrelated with the data mean; and (ii) is statistically homogeneous within the region affected by the filter. Then, two possibilities for estimating υ^2 arise. One possibility is the use of a constant value for the data mean, $\mu_0 = \tilde{\phi}(\boldsymbol{x})$, calculated for the point $\boldsymbol{x}$ placed at the centre of the region Ω_υ over which the average of the square fluctuation is estimated. Another possibility is the utilization of the local mean of the data, $\mu_k = \tilde{\phi}(\boldsymbol{x}_k)$, individually evaluated at all of the scattered points $\boldsymbol{x}_k$ used in the estimation of the variance. In the latter, the region affected by the local mean filter is translated so that the centre of Ω_F is placed at $\boldsymbol{x}_k$. These two approaches result, respectively, in

$$\upsilon_a^2 = \frac{1}{M_p} \sum_{k=1}^{M_p} (\phi_k - \mu_0)^2, \qquad (2.17)$$

$$\upsilon_b^2 = \frac{1}{M_p} \sum_{k=1}^{M_p} (\phi_k - \mu_k)^2, \qquad (2.18)$$

where M_p is the total number of points within the region Ω_υ. It should be noted that the mean μ can be estimated using an interpolative filter g_I in (2.6) and that Ω_F

used for the evaluation of μ can differ from Ω_v utilized for v^2. Equations (2.17) and (2.18) can be interpreted as filters aimed at estimating the mean quadratic fluctuation for which a constant weighting function, equal to unity, has been selected. This is admissible if the fluctuation is assumed to be statistically homogeneous in regions equal to, or greater than, Ω_v. Of the two alternatives, (2.17) is the less computationally demanding. However, in order to avoid the contamination of v^2 by a biased difference $(\phi_k - \mu)$, (2.18) is recommended whenever the data mean μ varies substantially in Ω_v compared with the fluctuation in the field φ.

3. Spectral analysis of accuracy

A means of characterizing the accuracy of the filtered data from homogeneously distributed, but randomly positioned, points is presented in this section. In order to do this, a statistical value of the relative error of the filter output is defined, and the contribution of the sine transformation components to the relative error is assessed.

3.1. *Accuracy of interpolative filters*

Generalizing the approach by Agüí & Jiménez (1987), the accuracy of interpolation can be characterized in terms of the following definition of the relative total error:

$$E_I = \frac{\left\langle \left(\varphi(\boldsymbol{x}) - \tilde{\phi}(\boldsymbol{x}) \right)^2 \right\rangle_{\psi,k,\varepsilon}^{1/2}}{\left\langle \varphi(\boldsymbol{x})^2 \right\rangle_{\psi}^{1/2}} \tag{3.1}$$

where $\varphi(\boldsymbol{x})$ is the exact value of the field φ at position $\boldsymbol{x}$ (not necessarily coincident with data points $\boldsymbol{x}_k$), and $\tilde{\phi}(\boldsymbol{x})$ is the estimation of φ using the interpolative filter g_I in (2.6). The subscripts ψ, k and ε in (3.1) indicate that in E_I the statistical average samples the contributions arising from all possible values of the signal phase, ψ, and noise, ε, at each of the N_p sampled points located at positions k. The signal phases and the positions of the data points are assumed to have a constant probability distribution function over their defined ranges, which are $[0, 2\pi]$ for ψ, and all the region Ω_F for any of the data points $\boldsymbol{x}_k$. No correlation exists between phases at different coordinates or between different components of the sine transformation. The definition of the relative error in (3.1) entails some differences with regard to the error of scattered data interpolation used by Agüí & Jiménez (1987). The latter defined the error for a sampled signal in two dimensions having a single frequency and being unperturbed by noise. The effect of noise in the analysis of Agüí & Jiménez (1987) was incorporated in the relative error as an independent additive term unaffected by the selection of a particular weighting function, which in their case was of Gaussian type in a circular window. Here, the definition of the relative error in (3.1) is extended to include directly the effect of noise in the quadratic difference of the numerator, as done by others for filters applied to structured data on a regular mesh (e.g. Nogueira, Lecuona & Rodríguez 1997; Acosta-Iborra 2004). Also, the relative error in (3.1) refers to the complete spectrum of the sampled signal. Incorporation of the noise together with the full spectrum of the data has proved to be a very powerful tool in analysing a broad range of structured data filters (Acosta-Iborra 2004). For scattered data filters, the inclusion of the noise in (3.1), as will be shown, allows the complex interaction between the filter weighting function and the signal noise to be characterized.

The relative error defined in (3.1) can be numerically estimated by means of Monte Carlo simulations as in Agüí & Jiménez (1987). In the present work this is

performed not only for a selected set of the spectral indices L of the data and for random combinations of ψ and k, but also for all random realizations of the noise ε. However, it is also possible to obtain an analytical estimate of E_I by substituting (2.1), (2.4)–(2.6) and (2.8) into (3.1) and calculating the statistical average of any given phase and of any data point location:

$$\langle \cdot \rangle_\psi = \frac{1}{2\pi} \int_0^{2\pi} (\cdot) \, \mathrm{d}\psi, \tag{3.2}$$

$$\langle \cdot \rangle_k = \frac{1}{\displaystyle\int_{\Omega_F} \mathrm{d}\mathbf{x}} \int_{\Omega_F} (\cdot) \, \mathrm{d}\mathbf{x}_k. \tag{3.3}$$

After some manipulation detailed in the Appendix (which is available as a supplement to the online version of this paper at http://dx.doi.org/10.1017/jfm.2013. 401 or on request from the authors), the relative total error of interpolation from randomly positioned points can be expressed as:

$$E_I \approx \frac{\left[\displaystyle\sum_{L=0}^{\infty} \hat{\varphi}_L^2 \hat{e}_{I,L}^2 + 2^D \frac{G_I}{N_p - 1 + G_I} \sigma_\varepsilon^2 \right]^{1/2}}{\left[\displaystyle\sum_{L=0}^{\infty} \hat{\varphi}_L^2 \right]^{1/2}}. \tag{3.4}$$

Here $\hat{\varphi}_L$ is the sine transform component of the data unperturbed by noise, as presented in (2.1), N_p is the number of points affected by the filter and σ_ε is the standard deviation of the additive noise or stochastic signal contained in the available data ϕ. The value of G_I is related to the weighting function for the interpolative filter by:

$$G_I = V_F \int_{\Omega_F} g_I^2(\mathbf{x}) \, \mathrm{d}\mathbf{x}. \tag{3.5}$$

Finally, $\hat{e}_{I,L}$ is the relative spectral error of interpolation for the spectral components L,

$$\hat{e}_{I,L} \approx \left[a_{I,L} + b_{I,L} \right]^{1/2} \tag{3.6}$$

where

$$a_{I,L} = \frac{(1 - \delta_L)^2}{1 + \dfrac{G_I}{N_p - 1}}, \tag{3.7}$$

$$b_{I,L} = \frac{2(1 - \delta_L) G_I}{N_p - 1 + G_I}, \tag{3.8}$$

with δ_L being equal to the following pseudo-spectral-transform of the weighting function centred at the origin of coordinates:

$$\delta_L = \int_{\Omega_F} g_I(\mathbf{x}) \prod_{i=1}^{D} \cos(x_i F_{i,l_i}) \, \mathrm{d}\mathbf{x}, \tag{3.9}$$

remembering that the integration domain Ω_F in (3.5) and (3.9) is a region of x in which the filter $g_I(x)$ is non-zero. Equations (3.4) and (3.6) are not exact since the approximation in (2.8) has been used. Therefore, the larger the number of points in the filter, the more exact is the analytical expression for the relative error. It should be noted that (3.6) does not reduce to the similar expression when points are regularly spaced, because here we are averaging for all the possible locations of points, whereas for regularly spaced points averaging is not required since points are fixed in space with respect to the centre of the filtering window.

One of the advantages of the expression given in (3.4) is that it allows the relative error of the interpolation procedure to be estimated without an exact knowledge of the interpolated field, φ (provided that there is prior knowledge of the dominant frequencies in φ). This will be illustrated in § 4. Note that (3.4) is strongly influenced by the spectral relative error of interpolation $\hat{e}_{I,L}$, and therefore it is worth considering the implications of the terms in $\hat{e}_{I,L}$, (3.6).

(i) The term $a_{I,L}$ is related to the spectral inaccuracy of the filter, which consists of a bias error arising from the attenuation produced by the weighting function in the amplitude of the sine components of the data, i.e. the Fourier coefficients in (2.1). This effect is always present unless the weighting function is a Dirac function. According to (3.9), the higher the data frequency (the larger the value of l_i) the smaller is δ_L and the more pronounced the attenuation of the amplitude of the data.

(ii) The term $b_{I,L}$ relates to the effect of the discrete nature and non-symmetrical collocation of the data on the accuracy of the filter. The larger the number of data points used in the filter, N_p, the less important this term becomes in the spectral relative error.

It can also be seen that if $\delta_L \leqslant 1$, then $a_{I,L}$ and $b_{I,L}$ are always positive.

The second element in the numerator of (3.4) is the noise or stochastic signal amplification term, and is proportional to the variance of ε, σ_ε^2. Since G_I is also present in this element, it acts as an amplification factor. To see this, it should be noted that, since g_I obeys (2.7), a weighting function with g_I homogeneously distributed in Ω_F yields a value of G_I smaller than a weighting function with sharp gradients of g_I along one or more directions. This means that the less homogeneous is the weighting function, the larger is G_I and the more amplified is the noise or the stochastic signal in the filter output. Equation (3.4) also reveals that an increase of the average number of points affected by the filter reduces the impact of the noise in the filter output. This is a logical consequence: the larger the number of points, the more compensated will be the random error in the summation in (2.6). Although not exactly the same, the closed-form expression for E_I and its qualitative behaviour resembles that for filters acting on points regularly spaced on a fixed mesh (Acosta-Iborra 2004).

To illustrate the above, the relative total error for filtering data in a two-dimensional field, (2.3), is given by:

$$E_I \approx \frac{\left[\displaystyle\sum_{l,r=0}^{\infty} \hat{\varphi}_{l,r}^2 \hat{e}_{I,l,r}^2 + \frac{4G_I}{N_p - 1 + G_I} \sigma_\varepsilon^2 \right]^{1/2}}{\left[\displaystyle\sum_{l,r=0}^{\infty} \hat{\varphi}_{l,r}^2 \right]^{1/2}} \tag{3.10}$$
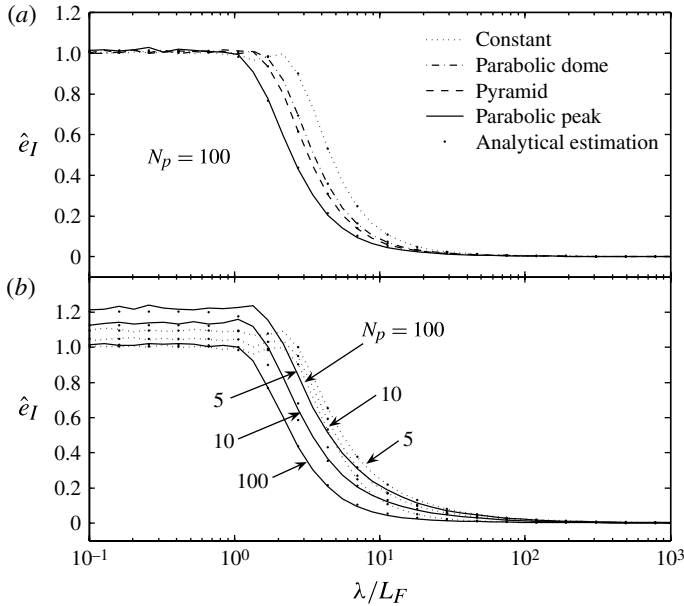
FIGURE 3. Monte Carlo results without noise ($\varepsilon_k = 0$), and analytical estimation (3.6), of the relative spectral error of interpolation versus the normalized spatial wavelength of an isotropic two-dimensional signal: (*a*) effect of the weighting function; (*b*) effect of the number of data points N_p, for the constant and parabolic-peak weighting functions only.

Source	$\delta_{l,r}$	G_I
Constant profile	$\operatorname{sinc}\left(F_{x,l}L_{F,x}\right)\operatorname{sinc}\left(F_{y,r}L_{F,y}\right)$	1
Parabolic dome	$\dfrac{9\left[\operatorname{sinc}\left(F_{x,l}L_{F,x}\right)-\cos\left(F_{x,l}L_{F,x}\right)\right]\left[\operatorname{sinc}\left(F_{y,r}L_{F,y}\right)-\cos\left(F_{y,r}L_{F,y}\right)\right]}{\left(F_{x,l}L_{F,x}\right)^2\left(F_{y,r}L_{F,y}\right)^2}$	$\dfrac{36}{25}$
Pyramid	$\operatorname{sinc}\left(\dfrac{F_{x,l}L_{F,x}}{2}\right)\operatorname{sinc}\left(\dfrac{F_{y,r}L_{F,y}}{2}\right)$	$\dfrac{16}{9}$
Parabolic peak	$\dfrac{36\left[1-\operatorname{sinc}\left(F_{x,l}L_{F,x}\right)\right]\left[1-\operatorname{sinc}\left(F_{y,r}L_{F,y}\right)\right]}{\left(F_{x,l}L_{F,x}\right)^2\left(F_{y,r}L_{F,y}\right)^2}$	9

TABLE 3. $\delta_{l,r}$ and G_I for some examples of two-dimensional interpolation filters. The function $\operatorname{sinc}(p)$ refers to $\sin(p)/p$ where p is a generic input value.

with $\hat{e}_{I,l,r} = \left[((1-\delta_{l,r})^2(N_p-1)+2G_I(1-\delta_{l,r}))/(N_p-1+G_I)\right]^{1/2}$. The expressions for $\delta_{l,r}$ and G_I are presented in table 3 for some two-dimensional weighting functions, $g_I(x,y) = h(x)h(y)$, generated from the functions h in table 1. Figure 3 shows $\hat{e}_{I,l,r}$ for the four examples of interpolative filters having the weighting functions presented in figure 2 and table 1. In figure 3, the horizontal axis indicates the spatial wavelength λ of each frequency of the spectrum of the scattered data in (2.3). This wavelength has been normalized by dividing it by half the size of the filter window, L_F. The

results correspond to a two-dimensional field having the same normalized wavelength in each spatial direction. That means the area of the filter window does not need to be a square, the only requisite being that $\lambda_x/L_{F,x} = \lambda_y/L_{F,y}$. For brevity, only this kind of *normalized isotropy* will be studied, although the results presented here are also applicable to anisotropic fields. In this sense, the results showing $\hat{e}_I$ in figure 3 are conservative if the normalized wavelength refers to the smaller of the two spatial coordinates in an anisotropic field. As figure 3(*a*) illustrates, the numerical estimation of $\hat{e}_I$ by Monte Carlo methods, described earlier in this section for an unperturbed data field with $\varepsilon_k = 0$, yields similar results to the analytical equation presented in (3.6), provided the number of scattered points affected by the filter, N_p, is not so small as to violate (2.8). For N_p equal to 10 and 5 (figure 3*b*), the discrepancy with the more exact Monte Carlo results reaches, respectively, 10 % and 20 % at low values of λ/L_F.

The value of $\hat{e}_I$ tends to zero when $\lambda \gg L_F$ because in that situation the data field is practically invariant within the window of the filter and the interpolation problem is trivial. The analytical expression deduced for the spectral relative error, (3.6), shows this fact: the pseudo-spectral-transform of the weighting function, δ_L, in (3.9) is equal to unity in a constant field ($\boldsymbol{L} = 0, 0$), which implies that the spectral inaccuracy a_I and the error due to the finite number of points b_I, both in (3.6), are null.

Obviously, the relative error increases when the spatial wavelength of the data is diminished. For example, if a normalized wavelength equal to 10 is chosen together with a number of points $N_p = 100$ within the filter window, figure 3(*a*) shows that all the filters tested, with the exception of the constant one, yield a spectral relative error $\hat{e}_I < 10$ %. The more homogeneous the weighting function of the filter, the smaller is δ_L (i.e. the more intensive is the smoothing effect of the filter) and, consequently, the larger is $\hat{e}_I$. For sufficiently small normalized wavelengths of the scattered data field, the relative spectral error approaches unity. Below a threshold value, λ_0, the relative error oscillates around unity, because the interpolation filter cannot accurately resolve spatial scales with wavelengths smaller than the size of the window, owing to the averaging effect always present in filters of finite size. In particular, for the constant weighting function, figure 3(*a*) shows that $\lambda_0/L_F \approx 2$. For the parabolic peak, the least homogeneous weighting function tested, the threshold of the spatial wavelengths is the smallest of the four filters, i.e. $\lambda_0/L_F \approx 1$, because the predominant values of g_I in a parabolic-peak filter window are concentrated in a smaller area than with the other filters.

The effect of the number of scattered points, N_p, within the filter window on $\hat{e}_I$ is illustrated in figure 3(*b*) for the two extremes of interpolative filters studied, namely using either constant or parabolic-peak weighting functions. It can be seen that reducing N_p always increases the spectral relative error of interpolation, with the filter using a parabolic peak being the more sensitive to N_p of the two considered. The analytical equation for $\hat{e}_I$ explains why this is the case: in (3.6) b_L is the term more affected by N_p, being inversely proportional to N_p and directly proportional to G_I. As discussed above, G_I increases with the degree of non-homogeneity of the interpolative weighting function. Thus, the relative error of interpolation also increases with the heterogeneity of the weighting function. The smaller the number of points the more probable it is that the points do not uniformly fill the window area, leading to a partial undetermination of the data field covered by the filter. If g_I is non-homogeneous, there is a risk that this partial undetermination might be accentuated. It should be noted, however, that for a given value of N_p the spectral relative error of interpolation always decreases in the order followed in table 1, that is, from constant to parabolic-peak filter.
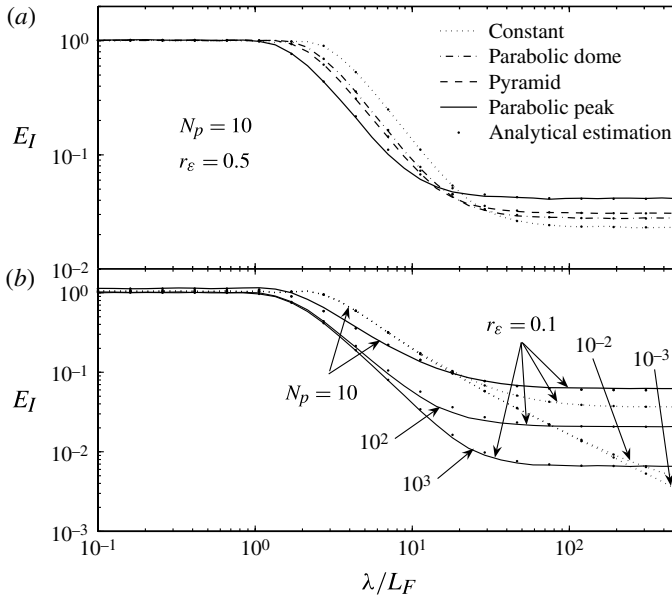
FIGURE 4. Monte Carlo results and analytical estimation (3.10), of the relative total error of interpolation versus the spatial wavelength of a single-frequency and isotropic two-dimensional signal perturbed with white noise: (*a*) effect of the weighting function; (*b*) effect of N_p and the noise-to-signal ratio r_ε.

The relative total error of interpolation (3.1) in a scattered data field affected by noise is presented in figure 4. Results in this figure are composed of Monte Carlo and analytical estimations of E_I. Additive white noise has been selected since it represents the most unfavourable measurement perturbation affecting the data. To reveal the contribution to the inaccuracy associated with each spatial wavelength of the data to be interpolated, a single-frequency field is studied in this figure. Thus, the Monte Carlo simulations undertaken for figure 4 are similar to figure 3 except that the former now has noise. The relative error in multi-frequency fields can be extrapolated from figure 4 by integrating the relative error of each spatial wavelength and assigning a level of noise or stochasticity to each data frequency. As figure 4(*a*) demonstrates, very good levels of agreement are obtained between the numerical results of the total relative error and the analytical approximation (3.10), even for a reduced number of data points N_p. In figure 4(*a*), a small value of N_p has been chosen in order to enhance the differences amongst the filters. The main distinction between the curves depicted in figures 3 and 4 is that the noise content of the signal in the latter figure prevents the relative total error approaching zero when the original data φ are smooth or constant, namely when $\lambda \to \infty$. Instead, for large wavelengths, it can be seen in figure 4(*a*) that E_I tends to a minimum limiting value, $E_{I,\infty}$, which is solely a result of the random white noise added to φ. From the analytical expression obtained for E_I in (3.4), the minimum relative error of interpolation can be deduced:

$$E_{I,\infty} \approx \left[\frac{2^D G_I}{3 \left(N_p - 1 + G_I \right)} \right]^{1/2} r_\varepsilon \tag{3.11}$$

where r_ε is the ratio of the maximum amplitude of the white noise, or stochastic signal, to the amplitude of the data φ, or deterministic signal, for each wavelength. Thus, with $\varepsilon \in \left[-r_\varepsilon \hat{\varphi}_L, r_\varepsilon \hat{\varphi}_L \right]$, then $\sigma_\varepsilon^2/\hat{\varphi}_L^2 = r_\varepsilon^2/3$. Equation (3.11) explains why, in figure 4(*a*), the more homogeneous the weighting function of the filter, the more accurate is the interpolation of a constant, or very smooth, data field affected by measurement noise. Filters possessing constant, or nearly homogeneous, weighting functions g_I yield smaller values of G_I than filters with sharp gradients in g_I. According to (3.11), reducing G_I is an effective way of diminishing $E_{I,\infty}$. Nevertheless, figure 4(*a*) demonstrates that the price paid when using interpolative filters with small G_I is a larger relative error at medium or small normalized spatial wavelengths. Equations (3.4) and (3.11) also show the obvious result that increasing the noise fraction r_ε increases the total relative error and hence its minimum value. On the other hand, increasing the mean number of points contained in the filter window, N_p, leads to a decrease in the total relative error. This is also illustrated in figure 4(*b*) for the constant and parabolic-peak filters, the former approaching $E_{I,\infty}$ for normalized wavelengths outside the selected range for the abscissa.

3.2. *Accuracy of differentiation filters*

The statistical relative error for filters devoted to the differentiation of scattered data is defined in a manner similar to that for interpolating filters in (3.1). However, instead of determining the value of the exact or deterministic data φ, the objective of the filter is to estimate the exact data differentiated along some coordinate and denoted by φ^d. Then:

$$E_D = \frac{\left\langle \left(\varphi^d(\boldsymbol{x}) - \tilde{\tilde{\phi}}(\boldsymbol{x}) \right)^2 \right\rangle_{\psi,k,\varepsilon}^{1/2}}{\left\langle \varphi^d(\boldsymbol{x})^2 \right\rangle_{\psi}^{1/2}} \tag{3.12}$$

where $\varphi^d(\boldsymbol{x}) = \partial\varphi/\partial x_1 = \sum_{L=0}^{\infty} \hat{\varphi}_L F_{1,l_1} \cos(x_1 F_{1,l_1} + \psi_{1,l_1}) \prod_{i=2}^{D} \sin(x_i F_{i,l_i} + \psi_{i,l_i})$ and $\tilde{\tilde{\phi}} = \partial\tilde{\phi}/\partial x_1$. Here $\partial\tilde{\phi}/\partial x_1$ is defined by (2.15), with x_1 being the coordinate chosen for the differentiation. As detailed in the online Appendix, using an approach analogous to that employed to derive the analytical expression for E_I, (3.4), the relative total error involved in differentiating data from randomly positioned points, E_D, is given by:

$$E_D \approx \frac{\left[\displaystyle\sum_{L=0}^{\infty} \hat{\varphi}_L^2 F_{1,l_1}^2 \hat{e}_{D,L}^2 + \frac{2^D(1 - N_p^{-1})G_D}{N_p - 1 + G_I}\sigma_\varepsilon^2 \right]^{1/2}}{\left[\displaystyle\sum_{L=0}^{\infty} \hat{\varphi}_L^2 F_{1,l_1}^2 \right]^{1/2}}. \tag{3.13}$$

In (3.13) $\hat{e}_{D,L}$ is the relative spectral error of differentiation:

$$\hat{e}_{D,L} \approx \left[a_{D,L} + b_{D,L} \right]^{1/2} \tag{3.14}$$

where

$$a_{D,L} = (1 - \delta_L)^2, \tag{3.15}$$

$$b_{D,L} = t_1 \delta_L + t_2 \delta_L^2 + t_3 \xi_L \alpha_L + t_4 \alpha_L^2 \frac{G_D}{F_{1,l_1}^2} + t_5 \frac{G_D}{F_{1,l_1}^2}, \tag{3.16}$$

in which

$$t_1 = \frac{2}{N_p}, \tag{3.17}$$

$$t_2 = \frac{-2 + 4N_p - 3N_p^2}{N_p^3}, \tag{3.18}$$

$$t_3 = -\frac{2(N_p - 1)^2}{N_p^3}, \tag{3.19}$$

$$t_4 = \frac{(N_p - 2)(N_p - 1)}{N_p^3}, \tag{3.20}$$

$$t_5 = \frac{(N_p - 1)}{N_p^2}, \tag{3.21}$$

$$\alpha_L = \prod_{i=1}^{D} \text{sinc}\left(L_{F,i} F_{i,l_i}\right), \tag{3.22}$$

$$\xi_L = \frac{V_F \int_{\Omega_F} g_D^2(\boldsymbol{x}) \prod_{i=1}^{D} \cos\left(x_i F_{i,l_i}\right) \, \mathrm{d}\boldsymbol{x}}{F_{1,l_1}^2}, \tag{3.23}$$

$$G_D = V_F \int_{\Omega_F} g_D^2(\boldsymbol{x}) \, \mathrm{d}\boldsymbol{x}. \tag{3.24}$$

It can be seen that G_D in (3.13) acts as an amplification factor for the noise, or stochastic signal, in differentiation filters. However, both (3.13) and (3.14) are approximate, because $\tilde{\tilde{\phi}}(\boldsymbol{x})$ is calculated with the approximation given in (2.15); also, it has been assumed in the derivation of $a_{D,L}$ and $b_{D,L}$ that the weighting function $g_I(\boldsymbol{x})$ in (2.15) is symmetrical along the direction of differentiation. As was the case with E_I, the spectral relative error of the differentiation filter, $\hat{e}_{D,L}$, contains two terms:

 (i) $a_{D,L}$, related to the spectral inaccuracy of the filter; and
(ii) $b_{D,L}$, which accounts for the inaccuracy arising from the finite number of points in the filter window.

It can be seen that, similar to the case with interpolation, the source of error in (3.13) due to the noise or stochastic signal amplification is proportional to σ_ε^2. However, the main difference with interpolation filters is that the error in differentiation is more sensitive to the noise content or stochastic nature of the data, since the amplification factor G_D is normally greater than G_I. Another notable distinction from interpolative filters is the explicit presence of the data frequency along the differentiation direction, F_{1,l_1}, dividing G_D in E_D, which indicates that the data noise affects the filter output with more intensity if the main frequencies of the data are small instead of large. This behaviour has been also reported for differentiation filters applied to structured data in one spatial dimension (Lecuona, Nogueira & Rodríguez 1998) and in multiple dimensions (Acosta-Iborra 2004). However, (3.13) is definitely more intricate than the analytical total relative error for the differentiation of structured data (Acosta-Iborra 2004). Also, from (3.23), the higher the frequency the less sensitive is the spectral error, $\hat{e}_{D,L}$, to the number of points.
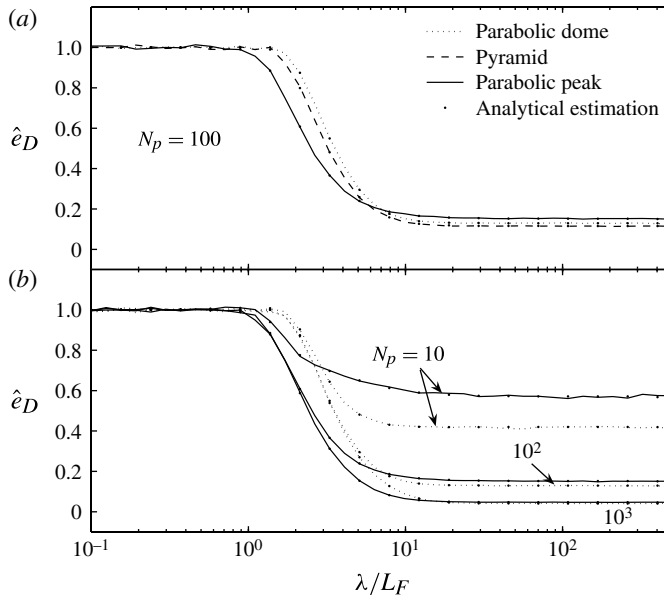
FIGURE 5. Monte Carlo results without noise ($\varepsilon_k = 0$) and analytical estimation (3.13), of the spectral relative error of differentiation versus the normalized spatial wavelength of an isotropic two-dimensional signal: (*a*) effect of the weighting function; (*b*) effect of N_p.

In two dimensions the spectral relative error of differentiation can be written

$$\hat{e}_{D,l,r} \approx \left[(1 - \delta_{l,r})^2 + t_1 \delta_{l,r} + t_2 \delta_{l,r}^2 + t_3 \xi_{l,r} \alpha_{l,r} + t_4 \alpha_{l,r}^2 \frac{G_D}{F_{x,l}^2} + t_5 \frac{G_D}{F_{x,l}^2} \right]^{1/2} \quad (3.25)$$

where $F_{x,l} = 2\pi l/S_x$ is the frequency of the data along the direction of differentiation. Expressions for $\xi_{l,r}$ and G_D are presented in table 4 for some examples of two-dimensional filters with a rectangular window and weighting function (2.16), constructed using h and h' from tables 1 and 2, respectively. Figure 5 depicts the relative spectral error of differentiation for the two-dimensional filters of table 4. In the figure, the relative spectral error has been evaluated using both a Monte Carlo method, imposing $\varepsilon_k = 0$, and the analytical approximation (3.13); it can be seen that the results are similar using either approach. Most of the comments made about figure 3 for interpolation are applicable to figure 5. Thus: (i) the spectral accuracy improves with an increase in the spatial wavelength of the data to be differentiated; (ii) results calculated with the parabolic-peak weighting function at medium spatial wavelengths are more accurate than the results from other more homogeneous weighting functions, as seen in figure 5(*a*); (iii) there is a threshold wavelength indicating that the filter cannot resolve scales smaller than the size of the window. However, an important difference arises between the relative spectral error of interpolation and differentiation filters. Statistically, the relative error of differentiation filters does not vanish for large wavelengths (namely in smooth data fields) even if they are free of measurement noise or stochasticity, as shown in figures 5(*a*) and 5(*b*). This fact contradicts the well-known behaviour of consistent filters acting over a regular grid of points, i.e. non-scattered data (Acosta-Iborra 2004; Ahnert & Abel 2007).

Source	$\xi_{l,r}$	G_D
Parabolic dome	$-162\dfrac{2\cos\left(F_{x,l}L_{F,x}\right)-2\text{sinc}\left(F_{x,l}L_{F,x}\right)+F_{x,l}L_{F,x}\sin\left(F_{x,l}L_{F,x}\right)}{\left(F_{x,l}L_{F,x}\right)^4}$ $\times\dfrac{3\cos\left(F_{y,r}L_{F,y}\right)-3\text{sinc}\left(F_{y,r}L_{F,y}\right)+F_{y,r}L_{F,y}\sin\left(F_{y,r}L_{F,y}\right)}{\left(F_{y,r}L_{F,y}\right)^4}$	$\dfrac{18}{5L_{F,x}^2}$
Pyramid	$32\dfrac{\text{sinc}\left(F_{x,l}L_{F,x}\right)\left[1-\text{sinc}\left(F_{y,r}L_{F,y}\right)\right]}{\left(F_{x,l}L_{F,x}\right)^2\left(F_{y,r}L_{F,y}\right)^2}$	$\dfrac{16}{3L_{F,x}^2}$
Parabolic peak	$2592\dfrac{\left[1-\text{sinc}\left(F_{x,l}L_{F,x}\right)\right]\left[6\text{sinc}\left(F_{y,r}L_{F,y}\right)+\left(F_{y,r}L_{F,y}\right)^2-6\right]}{\left(F_{x,l}L_{F,x}\right)^4\left(F_{y,r}L_{F,y}\right)^4}$	$\dfrac{108}{5L_{F,x}^2}$

TABLE 4. $\xi_{l,r}$ and G_D for some examples of two-dimensional differentiation filters.

Equation (3.14) can be used to explore the source of this unexpected inaccuracy when scattered data are differentiated. Since $\delta_L \to 1$ when $\lambda \to \infty$, the spectral inaccuracy related to $a_{D,L}$ does not contribute to $\hat{e}_{D,L}$ in these circumstances. Hence, $b_{D,L}$ is the source of error at long wavelengths so that the inaccuracy arises from the finite number of points. Despite the example weighting functions $h'(s)$ in table 2 being perfectly anti-symmetrical along s, neither the positions of points nor their density within the filter window are necessarily symmetrical. This generates a non-zero value in the result for the differentiation filter even in a data field containing constant values. Of course, the likelihood of having similar numbers of points placed at nearly symmetrical positions increases if the number of points covered by the filter window, N_p, increases. Therefore, as figure 5(b) and (3.14) demonstrate, $b_{D,L}$ decreases with N_p. Consequently, this inconsistency of the filter output at large spatial wavelengths (i.e. small frequencies) is an inherent flaw in differentiating filters dealing with scattered points. From figure 5(b), it is also clear that the inaccuracy arising from the finite number of points is less noticeable with weighting functions using a parabolic dome rather than a parabolic peak. This is because the more homogeneous the weighting function, the less amplified is the result of an unsymmetrical distribution of points along the direction of differentiation. Figure 5(b) clearly demonstrates that the result of differentiating data from scattered points is very sensitive to the number of points used by the filter, e.g. increasing from 14 % of minimum relative spectral error to more than 40 % when N_p is decreased from 100 to 10 in a window of a parabolic-dome filter. Thus, it is advisable not to differentiate when the number of points is small and the filter size cannot be increased.

Apart from the inaccuracy introduced by the finite number of points, the result from a differentiating filter is also very sensitive to the noise or stochastic signal content of the scattered point data. Figure 6 illustrates this fact. The curves depicted in figure 6 correspond to the relative total error, E_D, in differentiating a single-frequency, isotropic field using the three differentiating weighting functions of table 4. In contrast to the relative spectral error in figure 5, the total error in figure 6 grows without limit at large spatial wavelengths λ corresponding to the direction of differentiation. This is because, in (3.13), the term containing the standard deviation σ_ε of the stochastic component of the signal, increases with a decrease in F_{1,l_1}, which, in turn, is inversely proportional to the normalized λ. In other words, the increase in E_D at large data
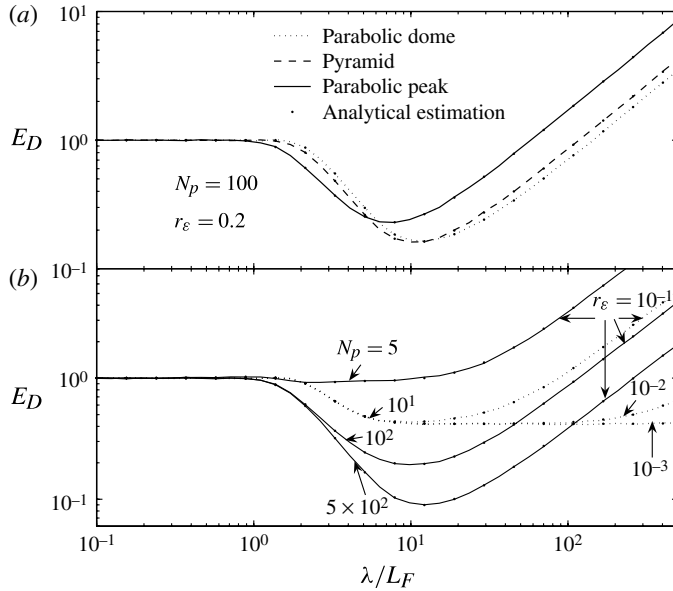
FIGURE 6. Monte Carlo results and analytical estimation (3.13), of the relative error of differentiation versus the spatial wavelength of a single-frequency and isotropic two-dimensional signal perturbed with white noise: (*a*) effect of the weighting function; (*b*) effect of N_p and r_ε.

wavelengths is produced by the amplification of ε perturbing the data φ. For data with a single frequency and perturbed by white noise, it is readily shown from (3.13) that the relative total error of differentiation at large values of λ is given by:

$$E_{D,\lambda \gg L_F} \approx \left[\frac{2^D (1 - N_p^{-1}) G_D}{12\pi^2 (N_p - 1 + G_I)} \right]^{1/2} \frac{\lambda}{L_F} r_\varepsilon \qquad (3.26)$$

where L_F is half the size of the filter window along the direction of differentiation. In figure 6(*a*), results from a Monte Carlo simulation as well as from (3.13) are depicted for $N_p = 100$ and additive white noise reaching up to 20 % of the harmonic amplitude of the tested field. At small or medium values of the normalized wavelength, there is only a reduced effect of the noise, as seen by comparing figures 5(*a*) and 6(*a*), because only the relative spectral error $\hat{e}_{D,L}$ predominates in that part of the spectrum. As the normalized wavelength increases, there is a balance between the decrease of $\hat{e}_{D,L}$ and the increase in the noise amplification, which can give a minimum in the curves of E_D, as figure 6(*a*) demonstrates. Thus, for given values of N_p and r_ε, there is an optimal range of λ defined by the statistical minimum in the E_D of a filter. The more homogeneous the weighting function used in the filter, the more displaced towards large values is the range of optimum λ, since both the amplification of noise and the spectral accuracy are smaller. This can be seen in figure 6(*a*). It should be noted from figure 6(*b*) that the minimum does not occur if the number of points affected by the filter window is too small. Again, the analytical estimation of E_D in (3.14) provides an explanation: a decrease of N_p simultaneously enhances the noise amplification and the spectral error in (3.13), smoothing and translating the minimum towards lower values of the normalized spatial wavelength until the minimum disappears. Obviously,

an increase in r_ε affecting the data elevates the total error, and results, eventually, in the extinction of optimal regions in E_D. This is exemplified in figure 6(*b*) for the parabolic-dome weighting function.

3.3. *Accuracy of variance filters*

When estimating the variance or mean quadratic fluctuation of stochastic data over the deterministic part of the data (i.e. the data mean), the statistical relative error associated with the estimation can be defined as:

$$E_\upsilon = \frac{\left\langle \left(\sigma_{\varphi'}^2 - \upsilon^2 \right)^2 \right\rangle_{\psi,k}^{1/2}}{\sigma_{\varphi'}^2}. \tag{3.27}$$

Here the estimated variance υ^2 is calculated either with the central mean (2.17) or with the local mean (2.18). In (3.27), the exact statistical mean of the quadratic fluctuation of the data is denoted by $\sigma_{\varphi'}^2$, which is the variance of the stochastic component of the data. In the present study of the relative error, only the situation in which the value of $\sigma_{\varphi'}^2$ is homogeneous along the data field will be considered. This can also be extended to cases where there is a small variation in $\sigma_{\varphi'}^2$ in the regions affected by the filter, Ω_F and Ω_υ. For simplicity, the noise is assumed to be either negligible compared to the stochastic fluctuation of the data, or, alternatively, is included in the fluctuation to be estimated. It is possible to derive an analytical expression for E_υ; however, the resulting expression is much more cumbersome than (3.4) or (3.13), and little advantage is gained from using it. For this reason, in the present study, only Monte Carlo simulations are used to assess the statistical relative error of variance filters.

Figure 7 presents the relative total error of the variance, E_υ, in a synthetic field composed of a isotropic data with a single-frequency mean or deterministic signal, φ, plus added stochastic data φ' consisting of white noise:

$$\phi_k = \varphi(\boldsymbol{x}_k) + \varphi'(\boldsymbol{x}_k). \tag{3.28}$$

Therefore, the purpose of the variance filter is to estimate the standard $\sigma_{\varphi'}^2$ of the random signal φ'. It should be recalled that the deterministic signal φ is estimated by the mean μ of the total data ϕ by means of an interpolative filter of size Ω_F, whereas the quadratic fluctuation is computed through (2.17) or (2.18) using the points within a region of size Ω_υ. The exact mean quadratic fluctuation is equal to $\sigma_{\varphi'}^2 = r_\upsilon^2 \hat{\varphi}^2 / 3$, where $\hat{\varphi}$ is the amplitude of the mean value signal and $r_\upsilon = \hat{\varphi}'/\hat{\varphi}$ the ratio between the maximum amplitude in the fluctuation and the mean of the data.

In figure 7, the horizontal axis represents the normalized spatial wavelength of the single-frequency deterministic data φ. For simplicity, the ratio $r_L = L_F/L_\upsilon$ has been chosen to be equal in both spatial directions, where $2L_F$ is the length of the window for the interpolative filter and $2L_\upsilon$ is that for the fluctuation calculation. The four interpolative filters for a rectangular window in table 1 have been employed in figure 7 for the calculation of μ. A small number of points, M_p, has been selected in figure 7(*a*) to enhance the differences between different curves. As figure 7(*a*) illustrates, the values of E_υ based on the central mean (2.17), are much larger than those based on the local mean (2.18). This is always true, except at large normalized wavelengths, for which the two approaches give similar results. Therefore, the use of the central mean (2.17) in the variance estimation should be avoided unless the
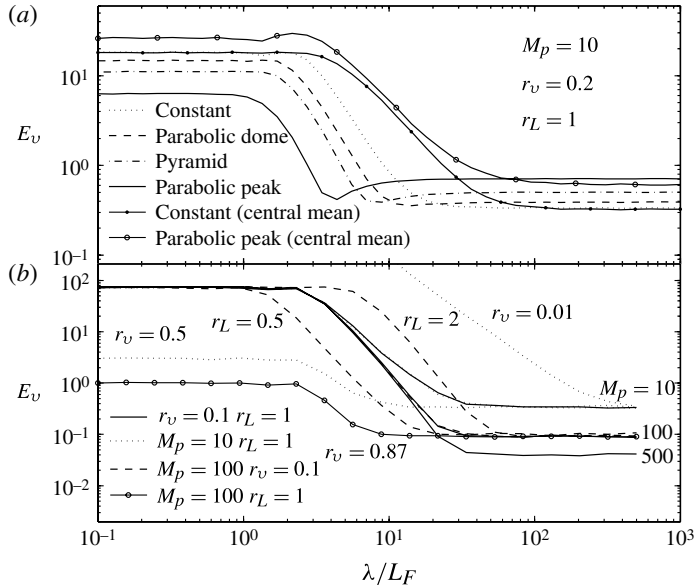
FIGURE 7. Monte Carlo results for the relative error E_υ in estimating the variance versus the spatial wavelength of a single-frequency and isotropic two-dimensional signal perturbed with white noise: (*a*) effect of the weighting function for μ; (*b*) effect of r_υ, r_L and M_p using a constant weighting function for μ.

scattered field of the mean signal φ is smooth or constant. In general the relative error increases if the normalized wavelength of the mean signal is decreased. This behaviour can be explained by re-examining figure 4(*a*), which indicates that the relative error of interpolation increases with a decrease in the normalized λ owing to the incapacity of filters to interpolate with accuracy deterministic data at scales close to the size of the window of the filter. In that situation, the error in estimating the deterministic data field with interpolative filters, $\mu = \tilde{\varphi}$, will contaminate the estimation of the variance in (2.17) and (2.18). The less homogeneous the weighting function, g_I, of an interpolative filter (e.g. parabolic peak), the smaller is E_υ at small wavelengths since the spectral accuracy of non-homogeneous filters is better than constant filters. However, at medium or large wavelengths, the random fluctuations of φ' are wrongly incorporated in μ, with this effect being accentuated by the non-homogeneity of g_I. These opposing effects at small and large wavelengths can lead to a minimum in the total error of the variance estimation, as seen in figure 7(*a*) for parabolic filters.

The effect of increasing the total number of points, M_p, used in (2.17) and (2.18) for the variance estimation is illustrated in figure 7(*b*). All the results in this figure have been calculated using a constant weighting function for the estimation of the mean data, but similar trends in the results can be obtained employing other kinds of weighting functions. As more points are used in the calculation of E_υ, the smaller is its value owing to the increased number of random samples. It should also be noted that for the same number of points, for example 100, the values of E_υ are clearly larger than the interpolation error presented in figure 3. Finally an interesting result in figure 7(*b*) is that maintaining the number density of scattered points constant, a reduction of r_L leads to a reduction in E_υ. This means that the improvement of the spectral accuracy arising from a reduction of the interpolative window size
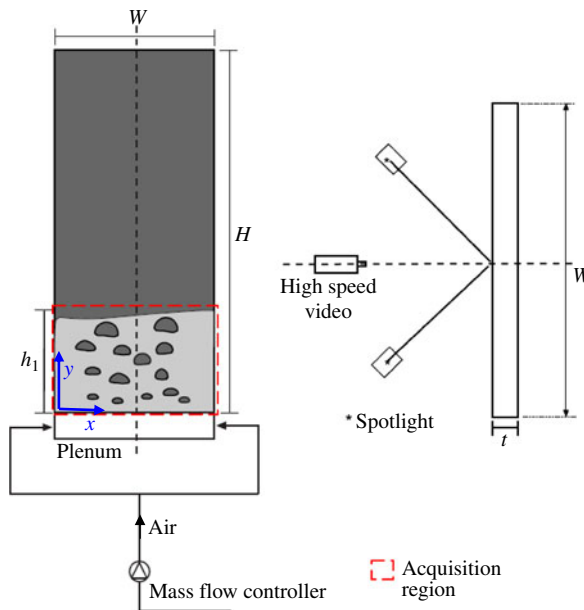
FIGURE 8. (Colour online) Schematic diagrams of the experimental apparatus employed for the image acquisition of bubbles in a two-dimensional fluidized bed.

dominates the growth of the uncertainty generated by the subsequent reduction of points within the interpolative window. Obviously, if the intensity of the random fluctuations increases with respect to the amplitude of the mean data φ in (3.28), namely r_v increases, the estimation of the variance is less affected by the inaccuracies associated with μ, and then the relative error E_v diminishes.

4. Application to bubble behaviour in gas–solid fluidized beds

To illustrate the application of the filters described above to a real system and to demonstrate how a methodical knowledge of the statistical error (figures 3–7) can facilitate the appropriate evaluation of experimental results, the spatial distribution, gradients and variance of the bubble size and velocity in a bubbling fluidized bed are characterized in the following section.

4.1. *Experimental apparatus and image processing*

The sizes and velocities of bubbles formed in a bed of particles, fluidized by air at ambient conditions, were measured. The bed was quasi-two-dimensional and is depicted in figure 8: it consisted of two vertical parallel plates, one made of glass the other of stainless steel, placed close to each other over an air distributor. The space between the two plates was sealed at their vertical edges, creating an internal volume of $50 \text{ cm} \times 200 \text{ cm} \times 0.5 \text{ cm}$ (width W, height H, and thickness t). The plates were sufficiently close together for most bubbles to bridge the 0.5 cm thickness and thus being only able to move in two dimensions. The particles were spheres made of glass with particle density 2500 kg m^{-3} and diameters in the range 600–800 µm. When fluidized by air at ambient conditions, these particles manifest Geldart Group B behaviour. The settled bed height was 30 cm. The distributor consisted of a thin plate containing 50 equi-spaced holes of 1 mm diameter. At ambient conditions, the
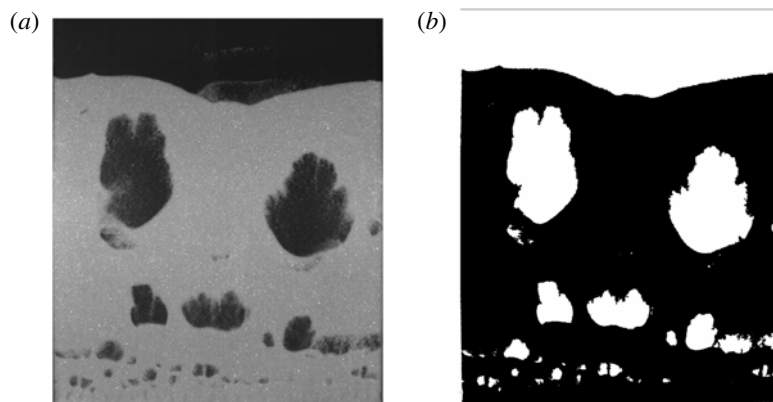
FIGURE 9. Example of an instantaneous image of the bubbling two-dimensional bed taken with a high-velocity CCD camera (*a*), and the detected bubbles (dark regions) after applying a threshold to the image (*b*).

Parameter	Value
Mean particle diameter	700 μm
Particle density	2500 kg s^{-1}
Minimum fluidization velocity of air, U_{mf}	0.34 m s^{-1}
Superficial air velocity, U_0	0.68 m s^{-1}
Height of the static bed	0.3 m
Total height of the bed container, H	2 m
Bed width, W	0.5 m
Bed thickness, t	5×10^{-3} m
Acquisition region dimensions, $h_1 \times W$	0.5×0.6 m^2
Total image size (pixels)	992×1270
Image exposure time	2 ms
Frames per second	125
Total number of frames recorded, N_{im}	3271

TABLE 5. Summary of the fluidized bed characteristics and the measurement technique employed.

superficial velocity of the air required for minimum fluidization, U_{mf}, was determined, by measurement of pressure drop across the bed, as 0.34 m s^{-1}. In keeping with a Geldart Group B material, bubbling occurred at superficial velocities just in excess of this value. In the experiments described here, the superficial velocity was always $U_0 = 2U_{mf} = 0.68$ m s^{-1}. A summary of the main operating conditions is given in table 5.

As shown in figure 8, images of bubbles were recorded by a CCD camera (Readlake Motion pro X3), which took $N_{im} = 3271$ sequential pictures (images) of the bed through the front glass plate, at a rate of 125 frames per second. Two 650 W spotlights were used to illuminate the particles in the bed. A typical frontal view of the bubbling bed is shown in figure 9(*a*), with the dark areas being the bubbles and the light areas the particulate phase. The dimensions of the images taken by the CCD camera were 992×1270 pixels (width $\times$ height): further details of the acquisition of images are given

in table 5. The images of the bubbling bed were processed using digital image analysis (DIA) techniques for the capture of bubbles and the quantification of their diameters and velocities (Sánchez-Delgado *et al.* 2008). To start with, a threshold filtering on the image grey levels was used to separate the bubbles from the particulate phase. This is exemplified in figure 9(*b*), which shows the threshold image resulting from the original image in figure 9(*a*). The DIA technique was able to eliminate the rain of particles visible inside bubbles in the images (seen in figure 9*a*). Bubbles of diameter <1 cm were rejected as their size is comparable to the bed thickness and therefore the bubbles and their surrounding particles may not be moving in two dimensions. In fact, these tiny bubbles constituted less than 15 % of the total number of bubbles captured and they were usually situated very close to the distributor where the fluidized bed cannot be considered two-dimensional.

After the threshold filtering, the positions of the centroids of the resulting selected bubbles, and their equivalent diameters $D_b = \sqrt{A_b 4/\pi}$, were determined. Here, A_b is the frontal area of a bubble as viewed by the camera. The velocity of each bubble was calculated from the displacement of its centroid between consecutive images using a standard time differentiation of second-order.

4.2. *Bubble number density*

A global field can be constructed by collecting all the centroid positions and assigning to them their equivalent diameter and velocity. Multiple bubbles originated at different positions along the complete set of images of the bubbling fluidized bed described in the previous section.

Over a given narrow increment of height above the distributor, the centroids of the bubbles can be assumed to be stochastic and uniformly distributed since the total time covered by the set of images was large, and the gas flow was evenly distributed. This global field was used to generate the results described below.

Figure 10 shows the mean number density of bubbles n_b at different vertical heights, y, above the distributor. Using the global field, the number density of bubbles was calculated as the total number of bubble centroids accumulated during all the acquisition time, placed inside a given region, and divided by the area of the region and the total number of images N_{im}. This yields an estimation of the most probable value of the instantaneous number of bubbles encountered per unit of frontal area in a region of the bed. Two different types of regions are tested in figure 10, all of them centred on the vertical axis of the bed, 0.25 m from either side. Type A windows were defined by an elongated region spanning the entire frontal width (0.50 m) of the bed: Type B regions were square. The dimensions of these regions are given in table 6.

It can be seen in figure 10 that the number density of bubbles grows rapidly up to a height slightly just above 0.05 m (i.e. ten times the bed thickness). This can be interpreted as the height, h_{tr}, of a transition region in which bubbles are created and grow to a size greater than the minimum bubble diameter required by the image analysis procedure. For heights greater than h_{tr}, the bubble density decreases with the height above the distributor, owing to bubble coalescence. The trend is reproduced by most of the types of windows tested in figure 10, except for size B3 ($2L_{F,x} \times 2L_{F,y} = 0.2$ m $\times$ 0.2 m, from table 6). This is to be expected because h_{tr} is significantly smaller than $L_{F,y}$ for B3 so that the presence of the peak in number density is not properly described. In general, the larger the size of the window used for averaging or filtering, the less resolved will be the resulting spatial profiles. In this sense, it can be seen that the intensity of the peak in n_b decreases with the size of $L_{F,y}$. It is interesting to note that n_b is quite similar for the profiles calculated with window
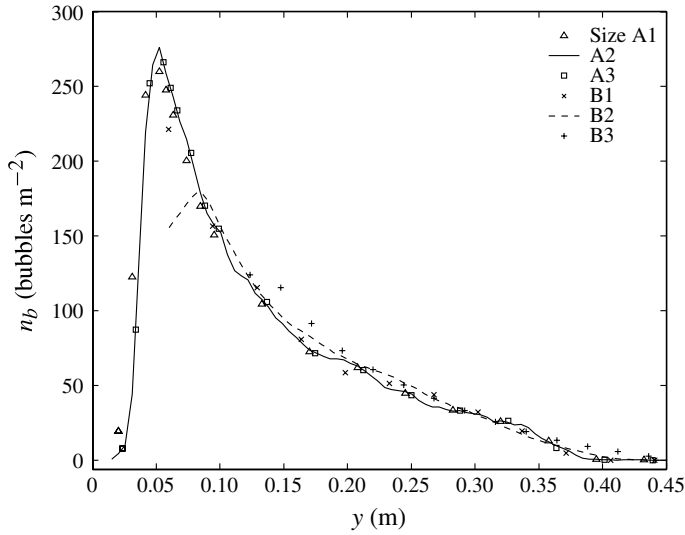
FIGURE 10. Experimental results of the bubble number density versus the height above the distributor of the bed obtained from different filter sizes (see table 6).

Size	$L_{F,x}$ (m)	$L_{F,y}$ (m)
A1	0.25	2.5×10^{-3}
A2	0.25	5×10^{-3}
A3	0.25	1×10^{-2}
A4	0.25	2.5×10^{-2}
A5	0.25	5×10^{-2}
A6	0.25	0.1
B1	2.5×10^{-2}	2.5×10^{-2}
B2	5×10^{-2}	5×10^{-2}
B3	0.1	0.1

TABLE 6. Dimensions of the rectangular filters used in the processing of
the experimental data.

sizes A3 and B1 except for y very close to h_{tr}. The fact that both sizes have nearly similar vertical widths, $2L_{F,y}$, but very different horizontal widths, $2L_{F,x}$, suggests that bubbles are homogeneously distributed along the entire width of the bed and therefore that the predominant gradient in n_b is oriented towards the vertical, rather than the horizontal, direction. This is corroborated by the map of n_b within the plane of the bed shown in figure 11(*a*). In this figure, the horizontal distance from the left-hand side is denoted by x.

Figures 10 and 11(*a*) can be used to determine the expected number of scattered data points N_p (namely bubble centroids) affected by the filter windows of table 6. These are calculated using $N_p = 4n_b L_{F,x} L_{F,y} N_{im}$. For the smallest sizes of window, N_p reaches a maximum value of $\sim$2100 data points (for size A2) and 1800 data points (for size B1) just above the transition region, and falling, for example, to $\sim$130 points

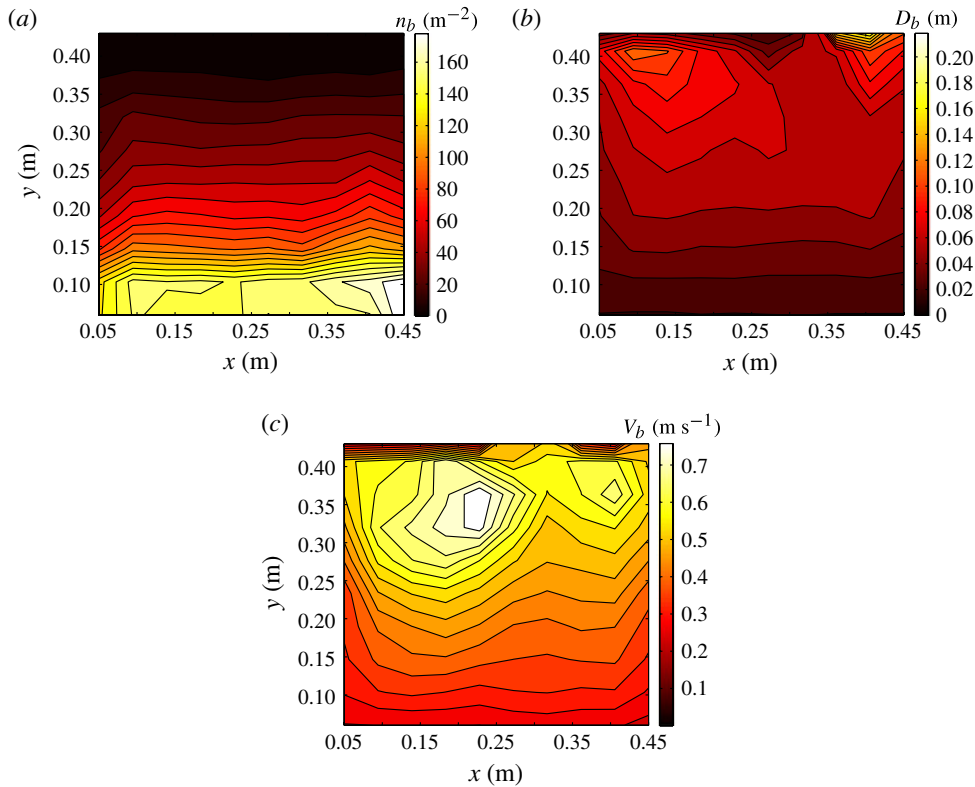FIGURE 11. (Colour online) Experimental maps of bubble number density n_b (*a*), equivalent diameter D_b (*b*) and vertical velocity V_b (*c*) calculated with a parabolic-dome filter of size B2.

(for both A2 and B1) at height 0.35 m. Thus, the number of scattered points available at 0.35 m is still usable for the data filtering.

4.3. *Bubble mean diameter and velocity*

Figures 11(*b*) and 11(*c*) present, respectively, a map of mean bubble diameter D_b in the bed plane and a map of mean vertical velocity V_b of bubbles in the same plane. The maps have been calculated using an interpolative filter with a parabolic-dome weighting function from table 1 with window of size B2 (0.1 m $\times$ 0.1 m, from table 6) applied over the global field containing the experimental results from all the images. In contrast to the number density of bubbles, figures 11(*b*) and 11(*c*) show that D_b and V_b vary noticeably along the horizontal direction x, especially in the upper part of the bed. This also confirmed by the horizontal profiles of D_b and V_b, given in figure 12, depicted for three different heights above the distributor. These mean data maps and profiles lose their symmetry for y far from the distributor, as noted by others (e.g. Shen, Johnsson & Leckner 2004). Since the images were collected over 30 s, and the number of bubbles in the upper regions of the bed is small, the distribution is less well sampled and the chance of obtaining an asymmetric sample is higher than for the lower regions of the bed.

The mean equivalent diameter of bubbles, and their mean vertical velocities, are shown as a function of the height y above the distributor in figure 13. These
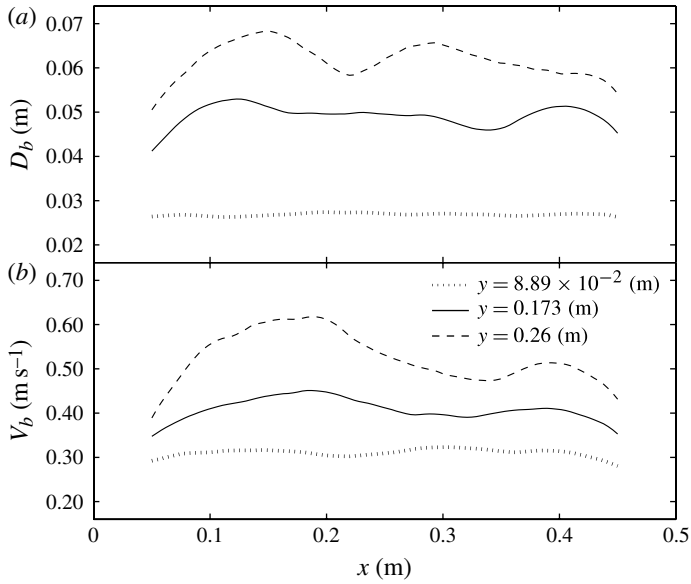
FIGURE 12. Experimental profiles of the mean bubble diameter (*a*) and vertical velocity (*b*) along the horizontal coordinate at three vertical distances from the distributor.
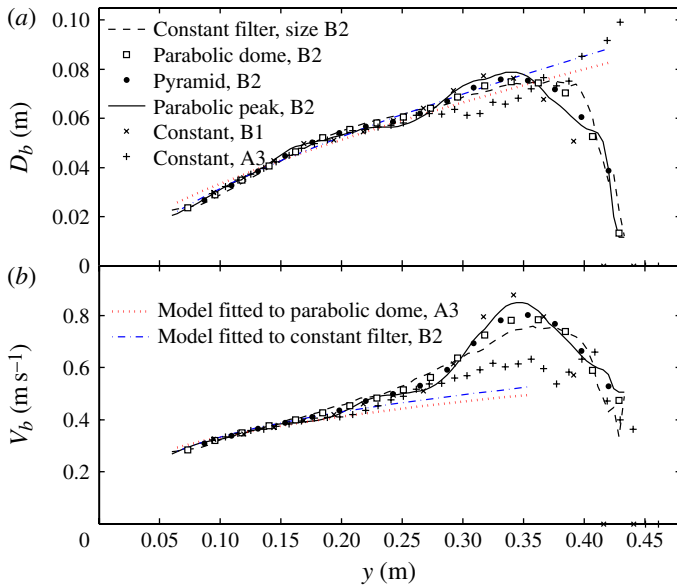

FIGURE 13. (Colour online) Experimental results for the mean bubble diameter (*a*) and vertical velocity (*b*) as a function of the height above the distributor.

experimental results have been calculated with interpolative filters based on different weighting functions, with the centre of the filtering window being placed on the central, vertical axis of the bed. Therefore, for the case of square filter windows of

type B, the results are representative of the data at the centreline of the bed and not in regions close to the lateral walls. For filters of type A, spanning the entire frontal width of the bed, the results correspond to data averaged along the horizontal direction. As figure 13 illustrates, both D_b and V_b increase with height for both types of window. It is well known that the growth of bubble diameter with height observed in figure 13(*a*) is primarily due to bubble coalescence (Darton *et al.* 1977), which is also corroborated by the decrease in the number density of bubbles in figure 10. The increase of D_b causes a corresponding increase in bubble velocity, cf. figures 13(*a*) and 13(*b*).

All the filters applied in figure 13 yield closely similar results up to heights of ∼0.25 m for D_b and 0.20 m for V_b. However, at heights greater than these, the mean values of the equivalent diameter and the bubble velocity are dependent on the size and nature of the weighting function employed. For example, at a height of 0.34 m, it is clear that, for filters of size B2, the constant weighting function gives curves with fewer oscillations and smaller maximum values of D_b and V_b than the parabolic-peak weighting function. This also happens with a constant weighting function used with windows of size B1 and A3, compared with the same function used with size B2. These observations can be interpreted in the light of the relative error curves for interpolation presented in figure 4. As explained in §3, the spectral accuracy of constant filters is lower than peak filters, indicating that the differences encountered between different filters in figure 13 arise from the presence of rates of change of D_b and V_b with height in the upper part of the bed being significant over distances close to, or smaller than, the size of the filter window B2. These gradients appear both in the vertical and the horizontal directions, since the results in figure 13 for the filter of size A3 present a smaller gradient and peak value in the upper half of the bed. Owing to these gradients, the results of bubble velocity based on local square filter windows (e.g. B2) in the upper half of the fluidized bed are clearly different to those involving the horizontal average (e.g. size A3), as figure 13 demonstrates.

Once the bubbles reach the free surface of the bed, at height $h_{bf} \approx 0.34$ m, they disappear from the measurements after eruption at the surface. This generates an apparent diminishing of the bubble diameter, since the centroid of small bubbles can reach higher values of *y* prior to eruption than can occur with large bubbles. This mechanism is reflected in figure 13, which shows a maximum in the curves for the mean bubble diameter and velocity. For example, taking the results from parabolic-dome filters shown in figure 13, the peak values of the bubble diameter and velocity are $D_b^* \approx 7.5$ cm and $V_b^* = 0.8$ cm, occurring at a similar distance from the distributor $h^* \approx 0.34$–0.35 cm. An abrupt decay of the mean equivalent diameter is observed in figure 13(*b*) at $y = 0.34$ m for all the filters tested. As this sharp decrease in the value of D_b is unambiguously defined and concentrated in a small range of vertical distances, it could be used as a novel means of defining the mean height h_{bf} of a bubbling bed. Thus, the bed height is defined by the height for which the extrapolated bubble size reaches zero diameter.

Using the Monte Carlo results or the analytical equation obtained for E_I, an estimate of the total relative error implicit in figure 13 was made. For example, according to figures 11(*b*) and 11(*c*), the smallest spatial scales (i.e. the largest gradients) are encountered near the peak values of D_b and V_b at $y = 0.35$–0.4 m. A rough estimate of the size of these scales can be made by assuming that the dominant spatial wavelength, λ, in the global field for D_b and V_b is the horizontal distance between two nearby peaks in figures 11(*b*) and 11(*c*), and twice the vertical distance between a peak and the freeboard. This gives a value between 0.10 and 0.3 m for the

horizontal wavelength, λ_x, and ~ 0.1 m for the vertical wavelength, λ_y. Consequently, interpolative filters of size B2 ($L_F = 0.05$ m) have a normalized wavelength between 2 and 6. As noted earlier, the number of bubbles at the height where the smallest scales are placed is approximately equal to 130. Selecting an intermediate wavelength $\lambda/L_F \approx 4$ and $N_p = 100$, the statistical relative error in the absence of measurement noise, from figure 3, is 25 % for the parabolic-dome filters, but 60 % if constant filters are used. Of course, the estimated relative error can increase with the presence of noise or the stochastic component of the data. Nevertheless, figure 4 indicates that the relative level of noise or stochasticity, r_ε, required to perturb the results at $\lambda/L_F \approx 4$ is high, especially for constant filters. It should be noted that filters of size A are nearly one-dimensional, as their height is much smaller than their width. Using (3.10), it is readily demonstrated that their embedded error in estimating the local value of D_b and V_b is principally affected by the gradients in the horizontal direction rather than in the vertical direction.

The interpolated results in figure 13 can be used to adjust parameters from theoretical models of D_b and V_b. Following a procedure analogous to the one used by Darton *et al.* (1977) for three-dimensional beds, it is possible to estimate the bubble diameter as a function of the height over the distributor in two-dimensional beds. This was done by Shen *et al.* (2004). However, a slightly different approach will be presented here, which explicitly accounts for the fraction, $\bar{\psi}$, of the excess gas, $U_0 - U_{mf}$, that passes through the bed as observable bubbles (Kunii & Levenspiel 1991), and for the virtual origin h_0 of bubble diameter. The following explains this new approach. There is a direct link between the equivalent diameter of each bubble in the bed and its velocity in the absence of other bubbles (Davidson & Harrison 1963), thus

$$V_b = \bar{\mu}\sqrt{gD_b} \tag{4.1}$$

where $\bar{\mu} = 0.71$ is a coefficient for an isolated bubble and $g = 9.81$ m s^{-2} is the gravity acceleration constant. This coefficient has been experimentally determined by Shen *et al.* (2004) for two-dimensional bubbling beds, as being between 0.8 and 1.0. Other recent investigations in two-dimensional beds, however, seem to indicate that $\bar{\mu}$ may be smaller than 0.71 (Busciglio *et al.* 2008), suggesting that the walls can reduce the bubble velocity over that for a single bubble far from walls or other bubbles (Glicksman, Lord & Sakagami 1987). Equation (4.1) was used by Darton *et al.* (1977), as well as by Lim, Gururajan & Agarwal (1993) and Shen *et al.* (2004), to build an analytical model describing the growth of bubbles as a function of their distance from the distributor. This was done in combination with the assumptions that the distance between two consecutive bubbles in the vertical direction is equal to $2\bar{\alpha}D_b$, with $\bar{\alpha} = 0.63$ for hemispherical bubbles, and that the vertical distance over which a bubble survives without coalescing is $\bar{\lambda}L_c$, where L_c is the characteristic separation between neighbouring bubbles in the horizontal direction. In two-dimensional beds $L_c = W/N_{tb}$ if bubbles are evenly distributed. Clearly, L_c is a function of the vertical distance above the distributor, y, because the instantaneous number of bubbles, N_{tb}, passing through a horizontal plane in the bed decreases with y owing to bubble coalescence.

The analytical models for bubble growth of Darton *et al.* (1977) and Shen *et al.* (2004) were deduced under the two-fluid assumption that all the gas in excess of that required for minimum fluidization, $U_0 - U_{mf}$, appears as bubbles. Further, in both studies, the expressions presented require knowledge of the conditions at the distributor, where $y = 0$. However, if only a proportion of the excess gas, $\bar{\psi}\left(U_0 - U_{mf}\right)$, is attributed to bubbles, and an arbitrary height, y_i, is used as the position for which the bubble conditions are known (so that y_i is not necessarily zero),

the following expression for the bubble equivalent diameter in a two-dimensional bed can be deduced, leaving other assumptions made by Darton *et al.* (1977) unchanged:

$$D_b^{3/2} = \frac{\bar{\alpha}\bar{\psi}}{\bar{\lambda}\bar{\mu}} \frac{8\left(2^{3/4}-1\right)\left(U_0 - U_{mf}\right)}{\pi g^{1/2}}\left[y - y_i + \frac{\bar{\lambda}A_i}{\left(2^{3/4}-1\right)t}\right]. \tag{4.2}$$

Here, $A_i = Wt/N_{tb}(y_i)$ is the horizontal sectional area of the bed at y_i per unit of bubble, with $N_{tb}(y_i)$ the number of bubbles in that horizontal section, and W and t are the nominal width and thickness of the bed. Equation (4.2) reveals that there is a virtual height, h_0, for which the bubble diameter is null, with $h_0 = y_i - \bar{\lambda}A_i/((2^{3/4}-1)t)$. It can be seen that h_0 might be positive or negative and acts as a virtual origin for the point at which the bubbles first start to grow: of course, it does not necessarily coincide with bubble formation in reality, because bubbles detach from the distributor with a non-zero size and their initial behaviour (i.e. for $y < h_{tr}$) might well not follow all the simplifying assumptions which led to (4.2).

From the point of view of parameter fitting, the expression presented in (4.2) has the interesting benefit that it permits the independent determination of parameters such as $\bar{\lambda}$, $\bar{\psi}$, or N_{tb}, and that y_i can be conveniently chosen on the basis of the experimental information available or the interest in a particular region of the bed. For example, figure 13(a) contains the analytical curves of the equivalent diameter, D_b, as a function of y resulting from a linear regression of (4.2) and the experimental results for D_b. The experimental results used for the regression came from: (i) a parabolic-dome filter of size B2 confined to the vertical line at the middle of the bed width; and (ii) a constant filter of size A3 representing the transverse average for the whole bed width. The regression of (4.2) using these filtered results in figure 13(a) provides the value of $\bar{\alpha}\bar{\psi}/\bar{\lambda}\bar{\mu}$ as well as h_0, and has been limited to the region $y \leqslant 0.3$ m because it appears that the local behaviour of the bed (especially for filters of size A3 and B1) deviates considerably near the upper surface of the bed, as discussed earlier. The regression of the data obtained from parabolic-dome filters B2 and constant filters A3 indicates that the virtual origin of bubble diameter is placed very close to the distributor, that is, at 1.29×10^{-2} m for the first filter and at -1.12×10^{-2} m for the second. These values are summarized in table 7 together with other resulting parameters.

By performing a standard least-squares regression, the experimental results for D_b and V_b presented in figure 13 were used to estimate values of the velocity coefficient $\bar{\mu}$ ranging from 0.581 to 0.599, as shown in table 8, for $y \leqslant 0.2$ m, i.e. sufficiently removed from the surface of the bed. This procedure is not intended for the estimation of the coefficient relating the instantaneous bubble diameter and velocity (in the range 0.8–1.0 as indicated previously), but the coefficient connecting their mean value for each distance over the distributor. Owing to the nonlinearity of (4.1), combined with the dispersion in bubble size encountered at any selected value of y, these two different approaches lead to different values. Using the empirically estimated value for $\bar{\mu}$, figure 13(b) depicts the model-fitted dependence of the mean bubble velocity on y computed after inserting (4.2) into (4.1). It should be noted that different results for the model-fitted velocity are obtained, depending on the filter employed in the estimation of the model parameters. In particular, the use of size A3 filters (transverse average) yields model parameters leading to smaller bubble diameters and velocities than filters with size B2 (local average at the bed centre).

Assuming a fraction of visible bubbles $\bar{\psi} \approx 0.65$, characteristic of bubbles formed in Geldart Group B particles (Kunii & Levenspiel 1991), and a vertical bubble separation, $\bar{\alpha} \approx 0.63$ (Darton *et al.* 1977), the regression of (4.2) in figure 13(b) gives $\bar{\lambda} \approx 2.00$

Parameter	Value
Bubbling bed height, h_{bf}	0.43 m
Transition region height, h_{tr}	0.052 m
Maximum mean bubble diameter, D_b^*	7.5×10^{-2} m
Maximum mean vertical velocity of bubbles, V_b^*	0.79 m s^{-1}
Vertical location of D_b^* and V_b^*, h^*	0.34 m
Maximum bubble growth near the activation region, $\left.\dfrac{\partial D_b}{\partial y}\right\|_{ac}$	0.25
Maximum bubble velocity increase near the activation region, $\left.\dfrac{\partial V_b}{\partial y}\right\|_{ac}$	1.6 s^{-1}
Maximum variance of D_b, $\left.\upsilon^2(D_b)\right\|_{max}$	2.2×10^{-3} m^2
Vertical location of $\left.\upsilon^2(D_b)\right\|_{max}$	0.4 m
Maximum variance of V_b, $\left.\upsilon^2(V_b)\right\|_{max}$	0.2 m^2 s^{-2}
Vertical location of $\left.\upsilon^2(V_b)\right\|_{max}$	0.35 m

TABLE 7. Main experimental results on bubble kinematics calculated with filters of size A2 (figure 10) and with parabolic-dome filters of size A5 and B2 (figures 13–15).

Parameter	Centre of the bed (size B2)	Transversal average (size A3)
$\bar{\mu}$	0.599	0.581
$\bar{\lambda}$	2.00	2.41
$\bar{\lambda}_{Shen}$	9.20	10.8
h_0	1.29×10^{-2}	-1.12×10^{-2}
$N_{tb}(y_i = 0.05$ m$)$	39.6	28.9

TABLE 8. Model parameters fitted with experimental data interpolated at the centre of the bed (filter of size B2) and data transversally averaged (size A3). $\bar{\alpha} = 0.63$ and $\bar{\psi} = 0.65$ have been selected for the calculations.

from the results interpolated with the parabolic-dome filter B2 and $\bar{\lambda} \approx 2.41$ from the constant filter A3. Although these values differ by $\sim 20\%$, they are of the same order as the constant $\bar{\lambda} \approx 1.17$ obtained by Darton *et al.* (1977) in their model for three-dimensional beds. It should be noted that if the fraction $\bar{\psi} \approx 0.65$ of visible bubbles were incorporated in that model, the results for the three-dimensional field would yield $\bar{\lambda} \approx 0.94$, which remains the same order of magnitude as $\bar{\lambda}$ from figure 13. In other studies, Shen *et al.* (2004) obtained $\bar{\lambda}_{Shen} \approx 6.5$ after applying their model to two-dimensional beds, and Almendros-Ibáñez *et al.* (2006), using the same model as Shen *et al.* (2004), found $\bar{\lambda}_{Shen} \approx 9.85$. Although these results appear to be unconnected to those obtained in the present work, by comparing (4.2) with the model presented by Shen *et al.* (2004), it is readily shown that both models are equivalent if $\bar{\lambda}_{Shen}$ is set equal to $\pi \bar{\lambda} \bar{\mu}/\bar{\alpha}\bar{\psi}$ and h_0 in (4.2) is substituted by $\bar{\lambda}\bar{\mu}A_i/\bar{\alpha}\bar{\psi} \left(2^{3/4} - 1\right) t$. This transformation of h_0 demonstrates that, although the models are not exactly the same, they are very similar on account of h_0 usually being small in magnitude. Therefore, ignoring the difference in h_0, the data contained in figure 13 provide $\bar{\lambda}_{Shen} \approx 9.20$–$10.75$, which is in excellent agreement with the results of Almendros-Ibáñez *et al.* (2006). As commented upon previously, it appears from figure 10 that bubbles are not completely formed, or their diameter is not large enough to be visible, in the transition region for $y < h_{tr}$, with $h_{tr} \approx 0.05$ m. In fact, figure 13(*a*) shows that
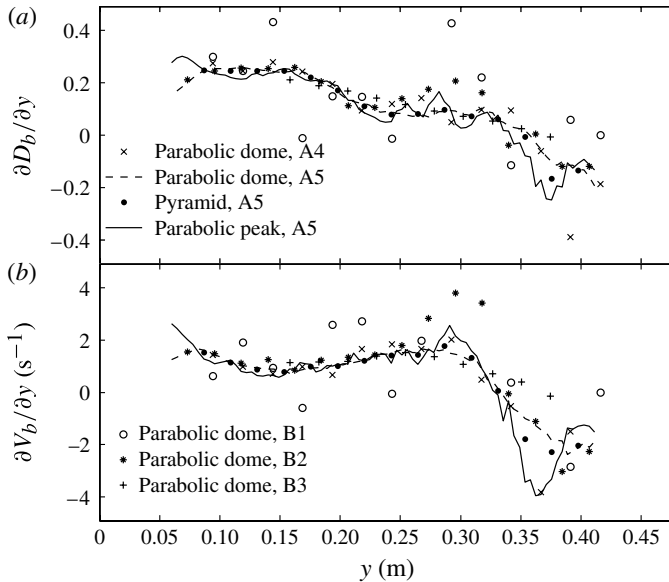
FIGURE 14. Experimental results for the mean derivative along the vertical direction of the bubble diameter (*a*) and vertical velocity (*b*) as a function of the height above the distributor.

bubbles have $D_b \approx 0.02$ m at $y = h_{tr}$. This confirms that it is not advisable to use (4.2) in the transition region, because the premises concerning two-dimensionality and gradual coalescence of bubbles do not hold for $y < h_{tr}$. Therefore, h_{tr} is the smallest value of y_i for which (4.2) is applicable in a two-dimensional bed. Extracting N_{tb} from the experimental value of the coefficient h_0 in table 8, the estimated number of bubbles crossing the horizontal section of the bed at $y = h_{tr}$ is 39.6 for parabolic-dome filters of size B2, and 28.9 for constant filters of size A3. These values seem realistic, since they are smaller than the number of orifices in the distributor. However, the two values differ from each other by more than 37 %, suggesting that the results are very sensitive to the selection of the filter and its size.

4.4. *Increment of bubble diameter and velocity with height*

The spatial derivative of the bubble diameter and velocity along the vertical direction for the two-dimensional bed is shown in figure 14. These experimental results have been calculated for filters of larger size than those used in figure 13. The objective of increasing the size of window of the filter was to attenuate the stochastic dispersion of the results. As demonstrated in § 3, the differentiation filters give results which are more sensitive to noise or other sources of fluctuation than interpolative filters. This can be seen in figure 14 by comparing the results for the filters of size A4 and A5. It can also be seen that, by examining results for filter windows of size A5, random fluctuations are damped more when the homogeneity of the weighting function (e.g. from parabolic peak to parabolic dome) is increased, as expected from results in figure 6. However, increasing the size of the filter also reduces the spectral accuracy of the derivative. For example, using filters of size B2 for $\lambda/L_F \approx 4$ and $N_p \approx 100$, an expected relative spectral error between 30 % and 45 % would be statistically obtained, as determined from figure 5, in the derivatives near the surface of the bed ($y \approx h^*$ in figure 14). If filters of size B3 are used instead, the estimated relative error increases

to between 60 % and 90 %. These indicate the sensitivity of the results to the size of the selected filter. Furthermore, in figure 14, it is clearly seen that the results obtained with a parabolic weighting function with size B3 (0.2 m × 0.2 m) follow a definite and smooth trend, whereas for smaller size B1 (0.05 m × 0.05 m) the results have a dispersed and random character. The only explanation for this observation is that the filter of size B1 is operating in the spectral region where the stochastic fluctuation of the data dominates over the mean value of D_b and V_b. This region is to the right of the minimum of E_D (figure 6a). In contrast, the filters of size B3 and (to a lesser extent) B2, are operating in a region in which the spectral error $\hat{e}_D$ is the largest contributor to the overall error, which is a region to the left of the minimum of E_D. A complete assessment of the relative total error in figure 14 cannot be done unless some estimate of the level of measurement noise or fluctuation is made. However, inspection of figure 6(a) reveals that if the noise were 20 % ($r_\varepsilon = 0.2$), the predicted statistical error for parabolic-dome filters of size B1 at $y \approx h^*$ (i.e. using $N_p = 100$ and $\lambda/L_F \approx 8$) would not be very much affected by the random fluctuation in the data values. Therefore, the level of fluctuation is probably greater than 20 % in that region of the bed since the size B1 filter shows significant fluctuation.

As figure 14 illustrates, the vertical derivatives of both D_b and V_b have the same trend. Up to $y \approx h^*$ (0.34 m from table 7) the derivative along the vertical direction is positive, indicating the coalescence and growth of bubbles coupled with their increase in velocity. For larger values of y, both derivatives in figure 14 become negative, so that both the mean bubble diameter and velocity decrease with increasing height above the distributor. As discussed earlier, this is probably due to larger bubbles erupting sooner than smaller ones. Obviously, the value of y at which the derivatives change sign coincides with the height, h^*, at which the peak values in D_b and V_b are located. Although not easy to see in figure 13(a), there appears to be a consistent reduction in the rate of growth of the mean bubble diameter with height, which can be clearly appreciated from figure 14(a). This reduction is probably the result of the fall in the bubble coalescence frequency, due to the increase in the horizontal separation between bubbles produced after each bubble coalescence (Darton *et al.* 1977) and which can be seen in (4.2). The reduction in bubble coalescence frequency is also in agreement with the progressively smaller gradient in the curve of n_b as y increases, as seen in figure 10. However, the derivative of the mean vertical velocity of bubbles with respect to y, shown in figure 14(b), does not manifest a clear trend for $y < h^*$. In fact, an interesting feature derived from figure 14(b) is that the vertical velocity of the bubbles does not seem to follow the progressive relaxation in the deceleration predicted by (4.1) for y near h^*. This occurs despite the fact that, as commented previously, (4.2) fits very well the mean bubble diameter. One possible reason, not reflected in (4.1) and (4.2), is that, on coalescence, the new bubble does not immediately begin to rise with its new velocity, but has to accelerate, as discussed by Müller *et al.* (2007). Since the time between successive coalescences increases with height (Darton *et al.* 1977), bubbles in the lower part of the bed have less time available to adjust their velocity according to their new volume after coalescence. This translates into derivatives of velocity in figure 14(b) that are smaller than those which would be obtained if the adjustment in the bubble velocity were instantaneous.

4.5. *Variance of bubble diameter and velocity*

As discussed earlier, the random values encountered in the experimental data for the bubble diameter and velocity can be produced by measurement noise or by the intrinsic stochastic behaviour of bubbling fluidized beds. Figure 15 presents the
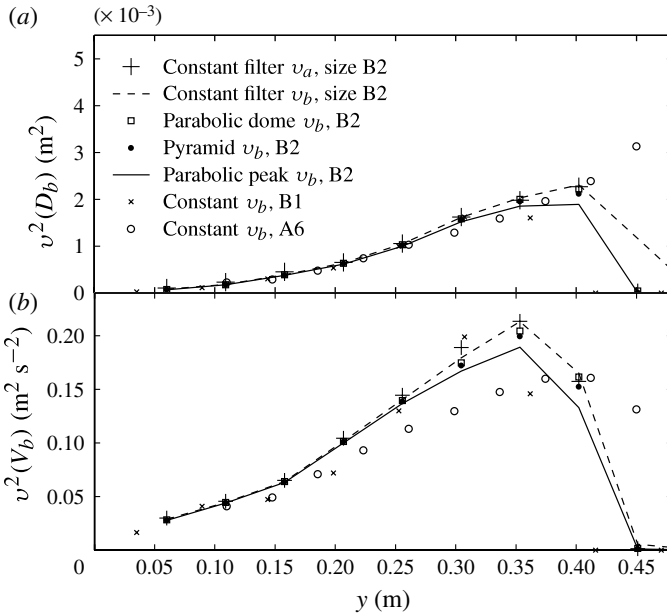
FIGURE 15. Experimental results for the variance of the bubble diameter (*a*) and vertical velocity (*b*) as a function of the height above the distributor.

vertical profiles of the mean quadratic fluctuation or variance of D_b and V_b at the middle of the bed (i.e. far from the lateral walls), calculated using (2.17) and (2.18) with $r_L = 1$. The profiles can be used to understand the cause of fluctuations in the experimental data in the fluidized bed studied. Figure 15 shows that there is a clear trend increase in the level of quadratic fluctuation of both diameter and bubble velocity with height up to $y \approx 0.40$ m for D_b and $y \approx 0.35$ m for V_b. These vertical distances define a maximum of variance for bubble diameter $\upsilon^2(D_b^*) \approx 2 \times 10^{-3}$ m^2 and for velocity $\upsilon^2(V_b^*) \approx 0.2$ m^2 s^{-2}. Despite the variance of D_b being two orders of magnitude smaller than the variance of V_b, their values relative to the mean presented in figure 13 are certainly similar. For example, comparing figures 13 and 15, the relative peak values of the mean square-root fluctuation are: $\sqrt{\upsilon^2(D_b^*)}/D_b^* \approx 0.6$ and $\sqrt{\upsilon^2(V_b^*)}/V_b^* \approx 0.56$, whereas at $y = 0.1$ m they respectively become 0.52 and 0.62. Therefore, the data dispersion in the bed, far from the walls, reaches a value of more than 50 % relative to their mean value, which translates to a dispersion range of $r_\upsilon \approx 0.5\sqrt{3} \approx 0.87$ if the probability distribution of the data values is assumed constant. This means that the bubble diameter and velocity constitute a highly stochastic phenomenon, and that this level of stochastic behaviour, relative to the mean value, does not depend on the height above the distributor. The qualitative similarity between the relative amounts of variance for D_b and V_b is due to the dependence of the bubble velocity on its diameter.

Figure 15 also indicates that the level of data variance attenuates near the walls, because the quadratic fluctuation for a filter covering the entire frontal width of the bed (size A6) is less intense than for local filters of smaller size in horizontal width, x (size B2). If the data variance were homogeneous in the x direction, the filters of larger size would yield greater quadratic fluctuation than filters of smaller size as a

consequence of the incorrect prediction of the data mean μ. A rough estimation of the accuracy in the calculation of the variance of D_b and V_b can be done with the Monte Carlo results presented in figure 7. Since the quadratic fluctuation is contaminated by the abrupt change in the mean data gradient at h^*, seen in figure 13, it is appropriate to use a filter of size B2 (0.05 m × 0.05 m). Thus, with $r_L = 1$, $N_p = 100$, $\lambda/L_F \approx 4$, and $r_\upsilon \approx 0.87$, figure 7 shows that $E_\upsilon \approx 0.3$ at h^*. This is a conservative estimate, since the changes in the spatial gradients of the mean D_b and V_b are less steep in the x direction than in the y direction. Besides, a smaller value of E_υ is expected since the effective r_υ that can be used in figure 7 is lower than 0.87 owing to the fact that the values of D_b and V_b possibly do not follow a constant probability function but a more realistic one concentrated towards their mean values. In agreement with the theoretical relative error of variance filters depicted in figure 7, the use of non-homogeneous weighting functions for the estimation of the mean μ in (2.17) or (2.18) yields in figure 15 lower values of the quadratic fluctuation than using a constant weighting function. For both $\upsilon^2(D_b)$ and $\upsilon^2(V_b)$, the quadratic fluctuation based on the global mean, υ_a^2, is very similar to that based on the local mean, $(\upsilon_b)^2$, which indicates that the means μ do not vary significantly through the filter area when compared with the significant fluctuations in D_b and V_b. As the bubble diameter and velocity are obtained by different processing techniques, it is unlikely that the level of fluctuation presented in figure 15 is caused by measurement and processing errors. In fact, random error caused by measurement noise and sub-pixel inaccuracy in placing the bubble centroid in the images is typically independent of the bubble size and position within the bed, so that it should be more homogeneously distributed than the fluctuations seen in figure 15.

5. Conclusions

The statistical accuracy of interpolation, differentiation and fluctuation filters acting on scattered data has been studied in this work. Novel analytical equations have been deduced for the estimation of the relative spectral and total error of interpolative and differentiation filters when applied to scattered data perturbed by noise or other sources of random signals. These analytical equations compare well with the results obtained from Monte Carlo simulations for the four examples of filter weighting functions considered: constant, parabolic dome, pyramid and parabolic peak.

Both the analytical and Monte Carlo results show that the relative spectral error of scattered data filters for interpolation and differentiation decreases if the higher values of the weighting function are concentrated towards the centre of the filter window. Using the analytical equations for the relative error, it has been possible to identify not only the sources of spectral inaccuracy, but also the noise amplification factors always present in the interpolation and differentiation of scattered data. In contrast to the behaviour of interpolative filters, the results have shown that the relative spectral error of differentiation filters does not vanish when the spatial wavelength is much larger than the filter window. To the authors' knowledge, the exact source of this unexpectedly resilient error has not been previously reported. It is produced by the random collocation of points within the filter window, which precludes the complete compensation of the null frequency terms to be differentiated, leading to inaccuracies that persist even for the trivial case in which the values of the sampled data are uniform. This inconsistency of the filter output, which becomes relevant at large spatial wavelengths (i.e. small frequencies), is inherent in differentiating filters dealing with scattered points. With regard to filters for estimating the variance of stochastic data,

the results demonstrate that the local mean approach (2.18) yields estimates of E_v subject to less relative error than the approach based on the central mean (2.17).

The scattered data filters were applied to a study of the distribution of bubble density, diameter and velocity in a two-dimensional gas-fluidized bed. Application of the filters has shown that bubbles are homogeneously distributed along the frontal width of the bed and that there is a transition region, close to the distributor, of height ∼10 times the bed thickness, in which departure from the standard two-dimensional behaviour occurs. A simple means of assessing the mean bed height h_{bf} of a bubbling bed has been proposed, making use of the sharp decrease observed in the mean bubble diameter at the upper surface of the bed. The results from the scattered data filters have also allowed the experimental evaluation of model parameters characterizing the bubble velocity and coalescence. To do this, the model of Darton *et al.* (1977) describing bubble growth has been modified to account explicitly for the fraction, $\bar{\psi}$, of the excess gas passing through the bed as observable bubbles. The modified model has led to the definition of a concept: the virtual origin of bubble diameter, h_0. The fitting of the model to experimental results has shown that the velocity coefficient, $\bar{\mu}$, i.e. the ratio between the rise velocity of an isolated bubble in a two-dimensional bed and $\sqrt{gD_b}$, has a value in the range $\bar{\mu} = 0.59$–0.61 using mean diameter and velocity. Also, the coalescence constant $\bar{\lambda}$ in the two-dimensional bed studied is of the same order as the value obtained by Darton *et al.* (1977) for three-dimensional beds. However, discrepancies between results obtained using different filters, reaching 20 % in $\bar{\lambda}$ and 37 % in the number of bubbles at a height 0.05 m from the distributor, indicate that there is sensitivity to the selection of the filter weighting function, and the size of its window. In this respect, the model adjusted with scattered points at the centre of the bed predicts slightly greater growths of bubble diameter and velocity than the one adjusted using interpolation data over the entire width of the bed.

The variance filters have revealed that the level of stochasticity of bubble diameter and velocity in the two-dimensional bed tested increases with the height above the distributor beyond that corresponding to the height of the unfluidized bed of particles. However, the relative level of stochasticity (i.e. square root of the variance divided by the mean values of diameter and velocity) is nearly constant with the vertical distance, having a value of order 50–60 % on the vertical central line of the bed, but attenuating near the lateral walls.

In conclusion, it has been shown that the observed behaviour of fluidized beds depends on the scattered point filter used and that previous knowledge of the statistical accuracy of scattered data filters is advisable for the adequate interpretation of the results. In fact, the analytical expressions and Monte Carlo results presented in this work could be used for the design of optimum interpolation and differentiation filters for a given frequency spectrum of a scattered data field.

Supplementary material

Supplementary material is available at http://dx.doi.org/10.1017/jfm.2013.401.

REFERENCES

ACOSTA-IBORRA, A. 2004 Auto-adaptive methods for the differentiation of velocity fields obtained from the particle image velocimetry (PIV) technique (in Spanish). PhD thesis, Universidad Carlos III de Madrid, Leganés, Spain.

AGÜÍ, J. C. & JIMÉNEZ, J. 1987 On the performance of particle tracking. *J. Fluid Mech.* **185**, 447–468.

AHNERT, K. & ABEL, M. 2007 Numerical differentiation of experimental data: local versus global methods. *Comput. Phys. Commun.* **177**, 764–774.

ALMENDROS-IBÁÑEZ, J. A., SOBRINO, C., DE VEGA, M. & SANTANA, D. 2006 A new model for ejected particle velocity from erupting bubbles in 2-d fluidized beds. *Chem. Engng Sci.* **61**, 5981–5990.

ANDERSON, T. B. & JACKSON, R. 1967 A fluid mechanical description of fluidized beds. *Ind. Engng Chem. Fundam.* **6**, 527–538.

ARMANINI, A., CAPART, H., FRACCAROLLO, L. & LARCHER, M. 2005 Rheological stratification in experimental free-surface flows of granular-liquid mixtures. *J. Fluid Mech.* **532**, 269–319.

BUNNER, B. & TRYGGVASON, G. 2002 Dynamics of homogeneous bubbly flows. Part 1. Rise velocity and microstructure of the bubbles. *J. Fluid Mech.* **466**, 17–52.

BUSCIGLIO, A., VELLA, A., GIORGIO, M. & RIZZUTI, L. 2008 Analysis of the bubbling behaviour of 2d gas solid fluidized beds. Part i. Digital image analysis technique. *Chem. Engng J.* **140**, 398–413.

DARTON, R. C., LANAUZE, R. D., DAVIDSON, J. F. & HARRISON, D. 1977 Bubble growth due to coalescence in fluidised beds. *Trans. Inst. Chem. Engrs* **55**, 274–280.

DAVIDSON, J. F. & HARRISON, D. 1963 *Fluidised Particles*. Cambridge University Press.

FOLEY, T. A. 1986 Scattered data interpolation and approximation with error bounds. *Comput.-Aided Geom. Des.* **3**, 163–177.

GLICKSMAN, L. R., LORD, W. K. & SAKAGAMI, M. 1987 Bubble properties in large-particle fluidized beds. *Chem. Engng Sci.* **42**, 479–491.

IMAICHI, K. & OHMI, K. 1983 Numerical processing of flow-visualization pictures – measurement of two-dimensional vortex flow. *J. Fluid Mech.* **129**, 283–311.

JACKSON, I. R. H. 1989 Radial basis functions: a survey and new results. In *The Mathematics of Surfaces* (ed. D. C. Handscomb), vol. III, Oxford University Press.

JACKSON, R. 2000 *The Dynamics of Fluidized Particles*. Cambridge University Press.

KUNII, D. & LEVENSPIEL, O. 1991 *Fluidization Engineering*. Butterworth-Heinemann.

LAZZARO, D. & MONTEFUSCO, L. B. 2002 Radial basis functions for the multivariate interpolation of large scattered data sets. *J. Comput. Appl. Maths* **140**, 521–536.

LECUONA, A., NOGUEIRA, J. I. & RODRÍGUEZ, P. A. 1998 Flowfield vorticity calculation using PIV data. *J. Vis.* **1**, 183–193.

LIM, K. S., GURURAJAN, V. S. & AGARWAL, P. K. 1993 Mixing of homogeneous solids in bubbling fluidized beds: theoretical modelling and experimental investigation using digital image analysis. *Chem. Engng Sci.* **48**, 2251–2265.

LÜTHI, B., TSINOBER, A. & KINZELBACH, W. 2005 Lagrangian measurement of vorticity dynamics in turbulent flow. *J. Fluid Mech.* **528**, 87–118.

MALIK, N. A. & DRACOS, T. H. 1995 Interpolation schemes for three-dimensional velocity fields from scattered data using Taylor expansions. *J. Comput. Phys.* **119**, 231–243.

MANN, J., OTT, S., PÉCSELI, H. L. & TRULSEN, J. 2005 Turbulent particle flux to a perfectly absorbing surface. *J. Fluid Mech.* **534**, 1–21.

MATTNER, T. W., JOUBERT, P. N. & CHONG, M. S. 2003 Vortical flow. Part 2. Flow past a sphere in a constant-diameter pipe. *J. Fluid Mech.* **481**, 1–36.

MÜLLER, C. R., HOLLAND, D. J., DAVIDSON, J. F., DENNIS, J. S., GLADDEN, L. F., HAYHURST, A. N., MANTLE, M. D., REES, A. C. & SEDERMAN, A. J. 2007 Rapid two-dimensional imaging of bubbles and slugs in a three-dimensional, gas–solid, two-phase flow system using ultrafast magnetic resonante. *Phys. Rev.* E **75**, 020302.

NAKAMURA, G., WANG, S. & WANG, Y. 2008 Numerical differentiation for the second-order derivatives of functions of two variables. *J. Comput. Appl. Maths* **212**, 341–358.

NOGUEIRA, J. I., LECUONA, A. & RODRÍGUEZ, P. A. 1997 Pdata validation, false vectors correction and derived magnitudes calculation on PIV data. *Meas. Sci. Technol.* **8**, 1493–1501.

ORPE, A. V. & KHAKHAR, D. V. 2007 Rheology of surface granular flows. *J. Fluid Mech.* **571**, 1–32.

POWELL, M. J. D. 1987 Radial basis functions for multivariable interpolation: a review. In *Algorithms for Approximation* (ed. J. C. Mason & M. G. Cox), pp. 143–167. Clarendon.

SÁNCHEZ-DELGADO, S., ALMENDROS-IBÁÑEZ, J. A., SORIA-VERDUGO, A., SANTANA, D. & RUIZ-RIVAS, U. 2008 Coherent structure and bubble-particle velocity in 2-D fluidized beds. In *Circulating Fluidized Bed Technology IX: Proceedings of the 9th International Conference on Circulating Fluidized Beds* (ed. J. Werther, W. Nowak, K. E. Wirth & E.U. Hartge), pp. 1007–1012. TuTech Innovation GmbH.

SHEN, L., JOHNSSON, F. & LECKNER, B. 2004 Digital image analysis of hydrodynamics two-dimensional bubbling fluidized-beds. *Chem. Engng Sci.* **59**, 2607–2617.

SHEPARD, D. 1968 A two-dimensional interpolation function for irregularly-spaced data. In *Proceedings of the 1968 23rd ACM National Conference (1968)* (ed. R. B. Blue & A. M. Rosenberg), pp. 517–524. ACM.

SPEDDING, G. R. & RIGNOT, E. J. M. 1993 Performance analysis and application of grid interpolation techniques for fluid flows. *Exp. Fluids* **15**, 417–430.

STICKEL, J. J. 2009 Data smoothing and numerical differentiation by a regularization method. *Comput. Chem. Engng* **34**, 467–475.

VEDULA, P. & ADRIAN, R. J. 2005 Optimal solenoidal interpolation of turbulent vector fields: application to PTV and super-resolution PIV. *Exp. Fluids* **39**, 213–221.

WEI, T. & LI, M. 2006 High order numerical derivatives for one-dimensional scattered noisy data. *Appl. Maths Comput.* **175**, 1744–1759.

WENDLAND, H. 2005 *Scattered Data Approximation*. Cambridge University Press.